



## **Final Draft** **of the original manuscript**

Hua, K.; Zhang, Y.; Kou, H.; Li, J.; Gan, W.; Fundenberger, J.; Esling, C.:

**Composite structure of  $\alpha$  phase in metastable  $\beta$  Ti alloys induced by lattice strain during  $\beta$  to  $\alpha$  phase transformation.**

In: Acta Materialia. Vol. 132 (2017) 307 – 326.

First published online by Elsevier: 25.04.2017

<http://dx.doi.org/10.1016/j.actamat.2017.04.051>

# Composite structure of $\alpha$ phase in metastable $\beta$ Ti alloys induced by lattice strain during $\beta$ to $\alpha$ phase transformation

Ke Hua<sup>a, b, d</sup>, Yudong Zhang<sup>b, d, \*</sup>, Hongchao Kou<sup>a</sup>, Jinshan Li<sup>a, \*\*</sup>, Weimin Gan<sup>c</sup>, Jean-Jacques Fundenberger<sup>b, d</sup>, Claude Esling<sup>b, d</sup>

<sup>a</sup> State Key Laboratory of Solidification Processing, Northwestern Polytechnical University, 710072 Xi'an, PR China

<sup>b</sup> Laboratoire d'Étude des Microstructures et de Mécanique des Matériaux (LEM3), CNRS UMR 7239, Université de Lorraine, 57045 Metz, France

<sup>c</sup> German Engineering Materials Science Center at MLZ, Helmholtz-Center Geesthacht, D-85748 Garching, Germany

<sup>d</sup> Laboratory of Excellence on Design of Alloy Metals for low-mAss Structures (DAMAS), Université de Lorraine, 57045 Metz, France

The  $\beta$  to  $\alpha$  phase transformation of Ti alloys progresses in a displacive diffusive mixed mode. The associated transformation strain has important influence on the resultant microstructure. In this work, the microstructural features of  $\alpha$  precipitates in a metastable  $\beta$  Ti alloy, Ti 7333, were thoroughly investigated. Special attention was paid to the intragranular  $\alpha$  for the advantage of a stress free transformation environment. Results show that the constituents of each  $\alpha$  precipitate is not single. Two kinds of nano sized  $\alpha$  domains exist. One is situated on the broad face of the major  $\alpha$  precipitate (named interface  $\alpha$ ), and the other goes through the major  $\alpha$  (termed penetrating  $\alpha$ ). The interface  $\alpha$  is related with the  $\beta$  matrix by the Burgers orientation relationship (BOR) and with the major  $\alpha$  by a  $60^\circ/(1120)_\alpha$  rotation. The nucleation of such  $\alpha$  particles is induced by the largest shear strain generated by the formation of the major  $\alpha$ . They act as stress associated sympathetic nuclei of the neighboring  $\alpha$  precipitates and eventually contribute to the formation of the triangular  $\alpha$  cluster. The penetrating  $\alpha$  does not obey the BOR with the  $\beta$  matrix but is related with the major  $\alpha$  by a  $60^\circ$  rotation around another  $(1120)_\alpha$  axis. The nucleation of such  $\alpha$  is induced by the largest normal strain generated by the formation of the main  $\alpha$  plate. This work provides comprehensive information on the displacive characters of the  $\beta$  to  $\alpha$  transformation and their impact on the microstructure of metastable  $\beta$  Ti alloys.

## 1. Introduction

The Al containing metastable  $\beta$  titanium alloys are considered as attractive materials for aeronautical applications due to their high yield strength, excellent fatigue crack growth resistance and good hardenability [1,2]. Their mechanical properties are strongly dependent on the microstructural characteristics, especially the volume fraction, the morphology and the distribution of  $\alpha$  precipitates [3–6], therefore the  $\beta$  to  $\alpha$  phase transformation has been a topic of intensive studies.

For the Al containing metastable  $\beta$  titanium alloys, the high temperature  $\beta$  phase with body centered cubic (BCC) structure

transforms to the lower temperature equilibrium  $\alpha$  phase with hexagonal close packed (HCP) structure when the alloy is slowly cooled across the  $\beta$  transus temperature ( $T_\beta$ ), or isothermally held at a temperature below  $T_\beta$ . Generally, the  $\beta$  to  $\alpha$  phase transformation involves two processes: diffusion of alloying elements and structure transformation of Ti atoms. The former results in a composition change of the product  $\alpha$  phase by depleting  $\beta$  stabilizing elements, such as Mo, Cr, Nb, and enriching  $\alpha$  stabilizing elements, such as Al, whereas the latter gives rise to the structure change from BCC to HCP [7–9]. Due to the displacive nature of the  $\beta$  to  $\alpha$  transformation, the transformation demonstrates specific crystallographic features, like the case of martensitic transformation. The transformation usually follows a certain orientation relationship (in most cases the Burgers orientation relationship (BOR), i.e.,  $\{110\}_\beta/\{0001\}_\alpha$ ,  $\langle 1\bar{1}\bar{1}\rangle_\beta/\langle 11\bar{2}0\rangle_\alpha$ ) with specific transformation habit plane [10,11]. The  $\alpha$  phase is usually in plate shape. A maximum of 12 crystallographic orientation variants can be produced due to the cubic symmetry of the parent phase and the

\* Corresponding author.

\*\* Corresponding author.

E-mail addresses: yudong.zhang@univ-lorraine.fr (Y. Zhang), ljsh@nwpu.edu.cn

BOR between the parent and the product phases. The transformation strain can be self accommodated by locally forming specific variants, giving rise to the appearance of characteristic microstructure patterns depending on the internal stress and the external stress conditions [12–19].

Recently, the displacive process of the  $\beta$  to  $\alpha$  transformation has been experimentally investigated in a Ti 5553 alloy [20]. It evidenced that at the very beginning of the transformation  $\alpha$  plates precipitate via a displacive process with a composition very close to that of the  $\beta$  matrix. Then they grow through a coupled displacive diffusional process with the partitioning of the alloying elements being transformation rate controlling [20]. The strain characters of the transformation and strain interaction between different variants have been analyzed theoretically [21–24]. It turns out that the transformation strain has strong influence on the formation of secondary  $\alpha$  particles and on local variant selection in relation to the need of minimizing the overall transformation strain energy.

Although the studies on the displacive characters of the  $\beta$  to  $\alpha$  transformation have greatly advanced our knowledge on the formation of specific microstructural features of the  $\alpha$  phase in Ti alloys, investigations on the constituents of individual  $\alpha$  precipitates and their correlation with the transformation strain are still limited. In view of such a situation, we conducted a thorough crystallographic study on  $\alpha$  precipitates, especially their sub structures, in a metastable  $\beta$  Ti alloy (Ti 7333) in the present work. The selection of this alloy is due to the fact that it demonstrates much faster  $\beta$  to  $\alpha$  transformation [25] and thus possesses more weighed displacive character for the transformation.

To obtain the  $\alpha$  precipitates produced by the displacive process of the transformation that happens at the very beginning of the formation of  $\alpha$  phase according to [20], the samples were aged very shortly after the over  $\beta$  transus solution treatment. In order to obtain the accurate transformation strain values, the lattice constants of the two phases were measured in situ by neutron diffraction at the transformation temperature.

## 2. Experimental details

The materials used in the present study is the Ti 7Mo 3Nb 3Cr 3Al (wt. %) (Ti 7333 [26]) alloy prepared first by multiple vacuum arc melting and then by forging in the  $\beta$  and the  $\alpha+\beta$  phase region. The composition was analyzed by capacity chemical analysis method and is given in Table 1. The  $\beta$  transus temperature measured by the metallographic method is approximately 850 °C.

Cylindrical samples with 15 mm in height and 10 mm in diameter were cut out of the center part of the forged Ti 7333 bar (150 mm in diameter). The samples were first solution treated at 900 °C in the  $\beta$  phase region for 30 min followed by water quenching to obtain a homogeneous single  $\beta$  microstructure. Then the solution treated samples were further aged at 700 °C for 5 min and quenched in ice water to allow one part of the  $\beta$  phase to transform to  $\alpha$  phase.

The lattice constants of the constituent phases at the aging temperature (700 °C) were measured in situ by neutron diffraction. The through volume measurements were performed with the neutron diffractometer STRESS SPEC located at a thermal beam port of FRM II in Garching, Germany. The Ge (311) monochromator was selected to produce neutrons with a wavelength of 1.618 Å. The

**Table 1**  
Chemical composition of Ti-7333 (wt. %).

Mo	Nb	Cr	Al	Fe	C	O	H	Ti
7.18	2.99	2.94	3.00	0.038	<0.1	0.11	<0.1	Bal.

bulk samples with dimensions of  $\Phi 5 \times 15$  mm were inserted into a vanadium crucible and immersed in the neutron beam with a size of  $5 \times 10 \times 10$  mm<sup>3</sup> under vacuum to prevent oxidation of the samples at elevated temperatures. The sample was heated to 700 °C and isothermally held for 50 min, and then cooled at a rate of 12 °C/min. A thermocouple was inserted from the top of the crucible to record temperature. Neutron diffraction patterns were collected in situ during isothermal holding and cooling at each 30 s. The  $(110)_\beta$  and  $(100)_\alpha$ ;  $(002)_\alpha$ ;  $(101)_\alpha$  diffraction peaks were captured at the detector position  $2\theta = 41^\circ$  with a detector window of  $15^\circ$ . The instrument parameters were fitted by the measurement of Si powder. The software StressTextureCalculator (STeCa) [27] was used to extract diffraction patterns.

Mesoscopic microstructural features were examined by scanning electron microscopy electron backscatter diffraction (SEM EBSD), using a JEOL 6500F SEM equipped with an EBSD acquisition camera and the Aztech online acquisition software package (Oxford Instruments). In order to achieve the surface quality required for EBSD measurements, the samples were first mechanically polished and then electrolytically polished with a solution of 5% per chloric acid in ethanol at a temperature lower than 15 °C and at 35 V for 15 s. The EBSD patterns were acquired at the accelerating voltage of 15 kV under beam controlled mode with a step size of 0.1  $\mu$ m.

The nano scaled microstructural and crystallographic features of the constituent phases were analyzed using a Philips CM 200 transmission electron microscope (TEM) operated at 200 kV. The TEM is equipped with a LaB6 cathode, a Gatan Orius 833 CCD camera, and homemade automatic orientation analysis software – Euclid’s Phantasies (EP) [28]. TEM thin films were prepared first by mechanical thinning to a thickness of about 70  $\mu$ m and then by electrolytic polishing to perforation at 25 °C in a solution of 5% perchloric acid in methanol at a voltage of 45 V, using a Struers Tenupol 5 twin jet electropolisher.

For TEM examination, the crystallographic orientation of the microstructural constituents were determined by indexing the TEM Kikuchi line patterns obtained in the nanoprobe mode using the software EP and expressed in a triplet of Euler angles in Bunge’s notation [29]. Orientation relationships (OR) between the microstructural constituents were analyzed by misorientation calculation. Dislocations were detected and analyzed by dislocation line match analysis method described in Ref. [30]. To avoid accidental match, at least 3 sample positions were used for each determination. The atomic correspondences between the parent  $\beta$  phase and the product  $\alpha$  phase were analyzed using the Crystal Maker<sup>®</sup> [31] software.

## 3. Results

### 3.1. Microstructure of the initial $\beta$ phase

Fig. 1(a) shows the microstructure of the solution treated Ti 7333 alloy that consists of equiaxed  $\beta$  grains with an average size of about 200  $\mu$ m. The disorientation angle distribution of the  $\beta$  grains is shown in Fig. 1 (b). It is seen that the  $\beta$  grains do not display any preferred crystallographic orientations or texture. Moreover, the amount of low angle disorientation ( $<5^\circ$ ) is very low, indicating that the  $\beta$  grains possess high crystalline perfection.

### 3.2. Lattice constants of the parent $\beta$ and the product $\alpha$ phase at the transformation temperature

Fig. 2 shows the diffraction pattern of the  $\beta$  phase and  $\alpha$  phase acquired at 700 °C (the aging temperature). Analysis of the diffraction data confirmed that the  $\beta$  phase has a BCC structure with lattice parameters  $a = 3.2471$  Å; whereas the  $\alpha$  phase possesses a

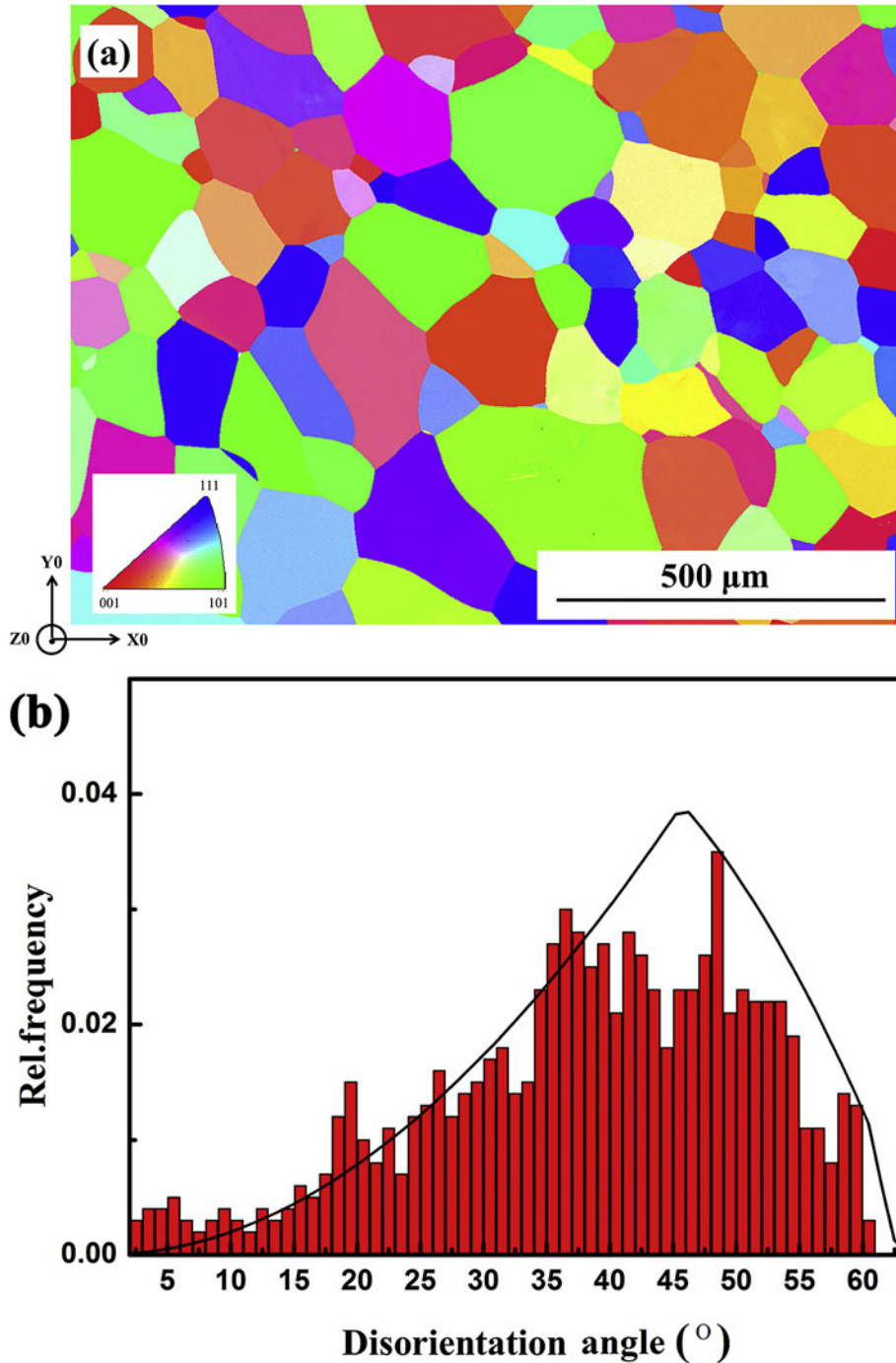


**Fig. 1.** (a) SEM-EBSD inverse pole figure (IPF) micrograph of the solution-treated Ti-7333 alloy and (b) Misorientation angle distribution of  $\beta$  phase.

HCP structure with lattice parameters  $a = 2.9340 \text{ \AA}$  and  $c = 4.6795 \text{ \AA}$ . The lattice constants of the two phases are slightly different from the data reported in Pearson's handbook [32]. This is due to the influence of the temperature and the alloying elements. The lattice constants will directly affect the lattice strain during the  $\beta$  to  $\alpha$  transformation. This part will be developed latter.

### 3.3. Microstructure characteristics of $\alpha$ precipitates

Fig. 3 shows the microstructure of the alloy after 5 min aging in  $\alpha + \beta$  phase region ( $700 \text{ }^\circ\text{C}$ ). It is seen that  $\alpha$  with lamellar shape

was precipitated in the  $\beta$  matrix. Three types of  $\alpha$  precipitates in terms of precipitation sites appear in the microstructure, namely, grain boundaries  $\alpha$  ( $\alpha_{GB}$ ), Widmanstatten  $\alpha$  ( $\alpha_W$ ) at the vicinities of  $\beta$  grain boundaries and intragranular  $\alpha$ . Further crystallographic analyses using EBSD orientation data demonstrate that the three types of  $\alpha$  precipitates possess the BOR with the surrounding  $\beta$  phase. These characters of  $\alpha$  in the present alloy are typical in the metastable  $\beta$  Ti alloys, such as Ti 5553 [33,34].

As in the present work we mainly explore the  $\beta$  to  $\alpha$  transformation in a stress free environment, we focused only on intragranular  $\alpha$  precipitates. Fig. 4(a) displays the intragranular  $\alpha$

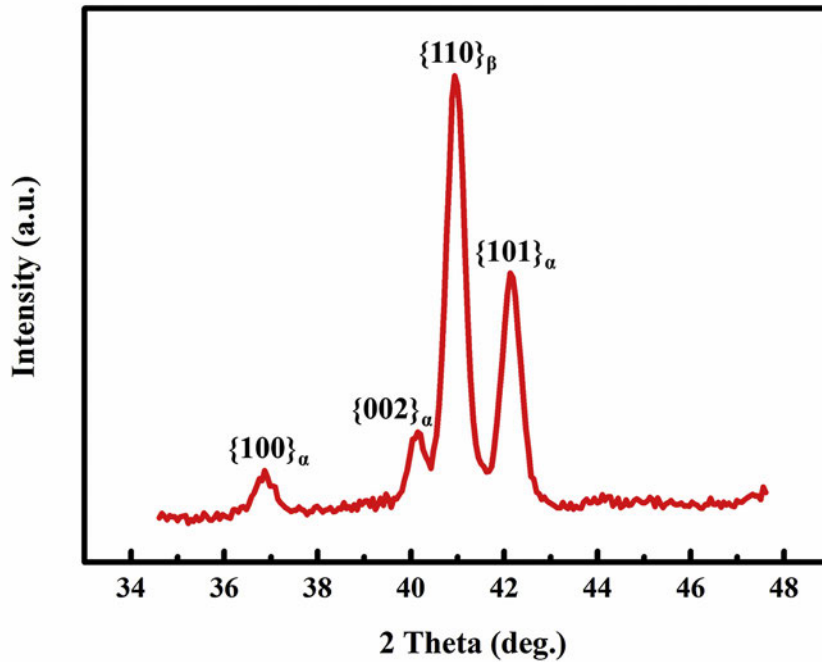


Fig. 2. Neutron diffraction pattern in the  $2\theta$  range  $34^\circ - 49^\circ$  of the Ti-7333 alloy acquired at  $700^\circ\text{C}$ .

precipitates in one  $\beta$  grain. In this case, the  $\langle 1\bar{1}1 \rangle_\beta$  of the  $\beta$  grain is perpendicular to the sample surface, thus 3  $\{110\}_\beta$  planes (the BOR planes) belonging to this axis zone are on edge, as shown by the  $\{110\}_\beta$  and  $\langle 1\bar{1}1 \rangle_\beta$  pole figures in Fig. 4(b). 12 BOR variants can be found in the  $\beta$  grain, as shown by the corresponding BOR plane and direction pole figures in Fig. 4(b). The disorientation between any two variants from the 12 variants belongs to the classic

disorientations of BOR variants, ie.  $10^\circ/\langle 0001 \rangle_\alpha$ ,  $60^\circ/\langle 11\bar{2}0 \rangle_\alpha$ ,  $60.8^\circ/\langle 1\bar{3}77 \bar{1} 2.377 0.359 \rangle_\alpha$ ,  $63.3^\circ/\langle 10 5 5 \bar{3} \rangle_\alpha$  and  $90^\circ/\langle 1 \bar{2}38 1.38 0 \rangle_\alpha$ . The habit plane of the intragranular  $\alpha$  was identified by matching the habit plane trace in the present alloy with the published habit planes in the literature [35–37] and were found to be close to  $\{11 11 13\}_\beta$ , as shown with the  $\{11 \bar{1}1 \bar{1}3\}_\beta$  pole figure in Fig. 4(c). Under such a specific  $\beta$  orientation, there are 3 variants

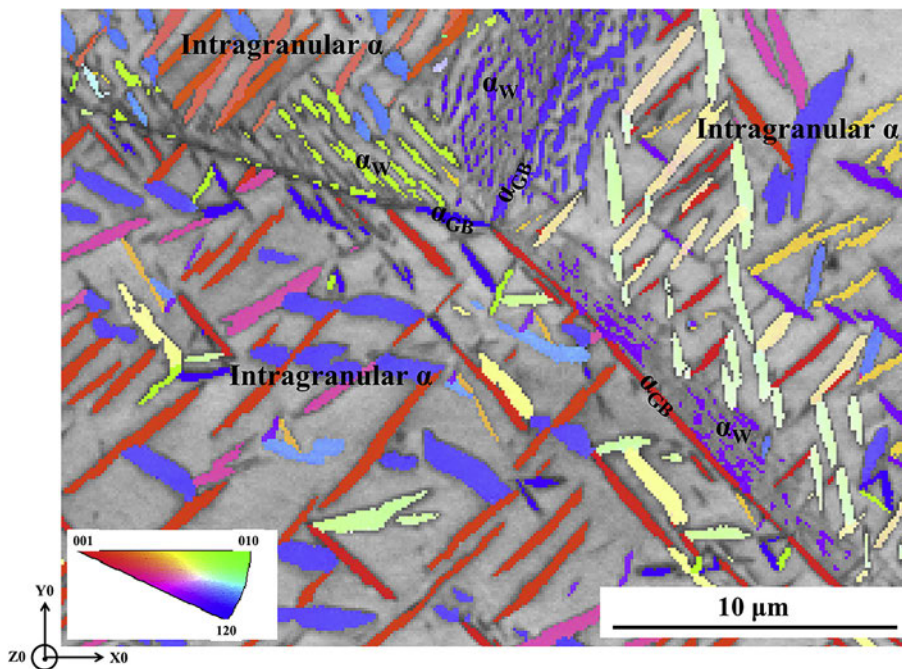
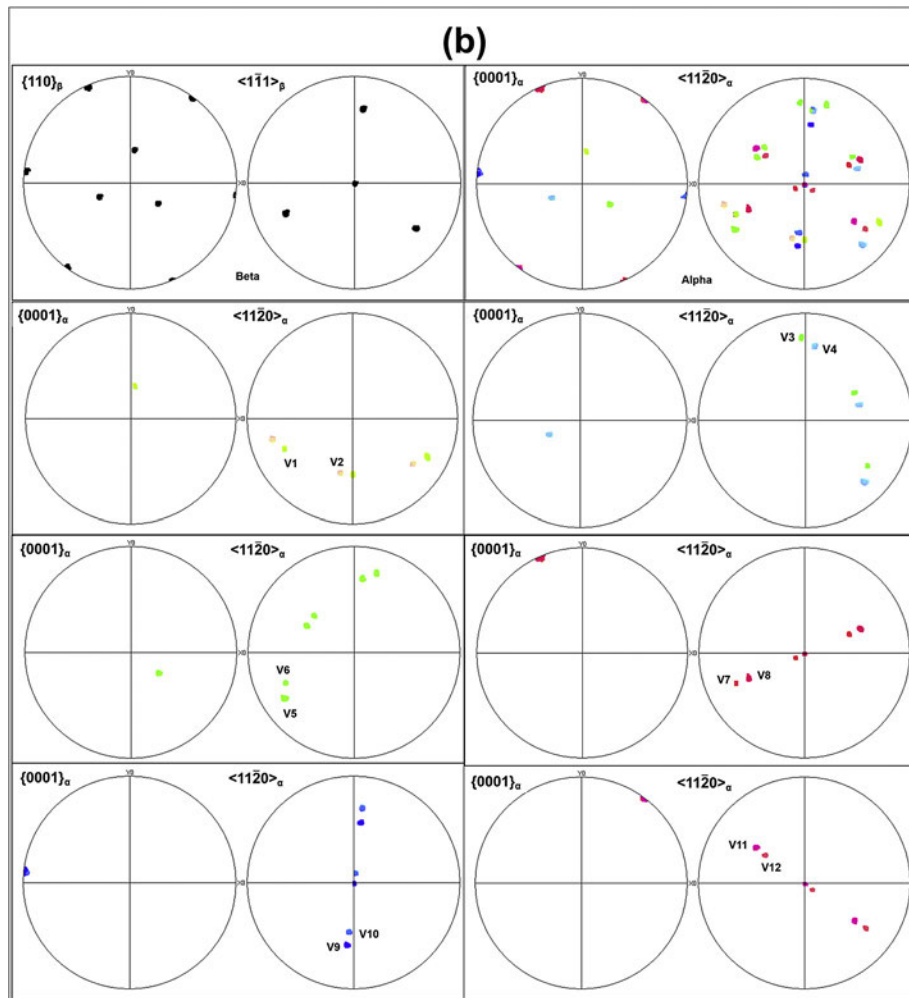
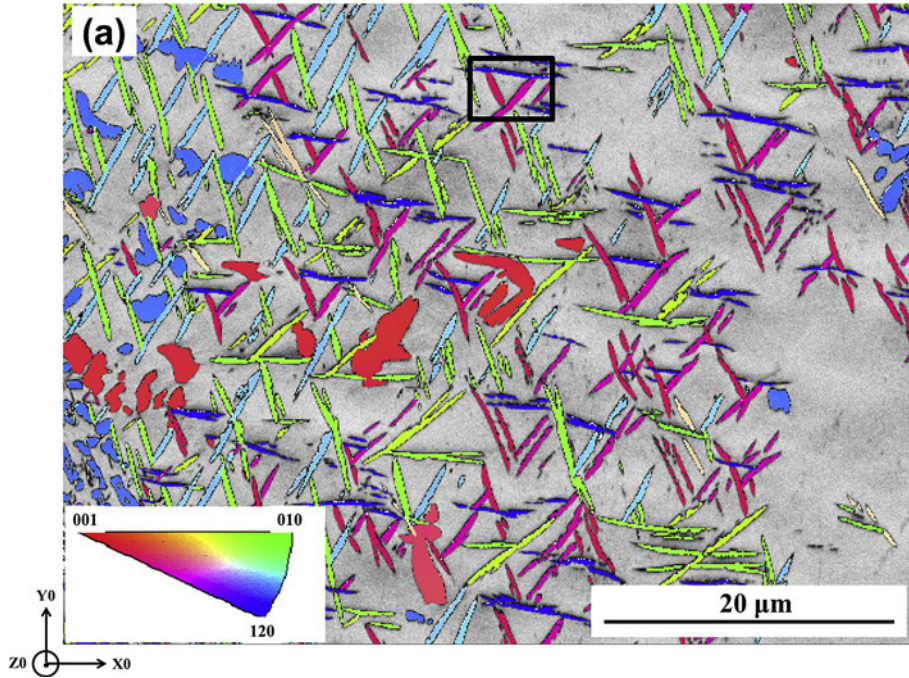


Fig. 3. SEM-EBSD micrograph of Ti-7333 alloy after solution treatment at  $900^\circ\text{C}$  for 30 min and aged at  $700^\circ\text{C}$  for 5 min demonstrating grain boundaries  $\alpha$  ( $\alpha_{GB}$ ), Widmanstatten  $\alpha$  ( $\alpha_w$ ) at the vicinities of  $\beta$  grain boundaries and intragranular  $\alpha$ . The  $\beta$  matrix is represented with its EBSD band quality contrast and the  $\alpha$  precipitates with their crystallographic orientation (expressed with the Z0 direction inverse pole figure (IPF)). The insert is the color code of the IPF.



**Fig. 4.** (a) SEM-EBSD micrograph of intragranular  $\alpha$  precipitates of Ti-7333 alloy after solution treatment at 900 °C for 30 min and aged at 700 °C for 5 min. The  $\beta$  matrix is represented with its EBSD band quality contrast and the  $\alpha$  precipitates with their crystallographic orientation (expressed with the Y0 direction inverse pole figure (IPF)). The IPF color code is inserted in the figure. (b) Corresponding BOR direction and plane pole figures of the  $\beta$  matrix and the 12  $\alpha$  variants. The poles of the  $\alpha$  variants are represented with the consistent colors in (a). (c)  $\{11\ \bar{1}\ \bar{1}\}_\beta$  (habit plane) pole figures with two specifically oriented  $\alpha$  plates for obtaining 3D morphology of the  $\alpha$  precipitates, and their 3D illustration. (d) BOR direction pole figures of the 3  $\alpha$  variants forming the triangular structure and BOR direction pole figure of the parent  $\beta$ .

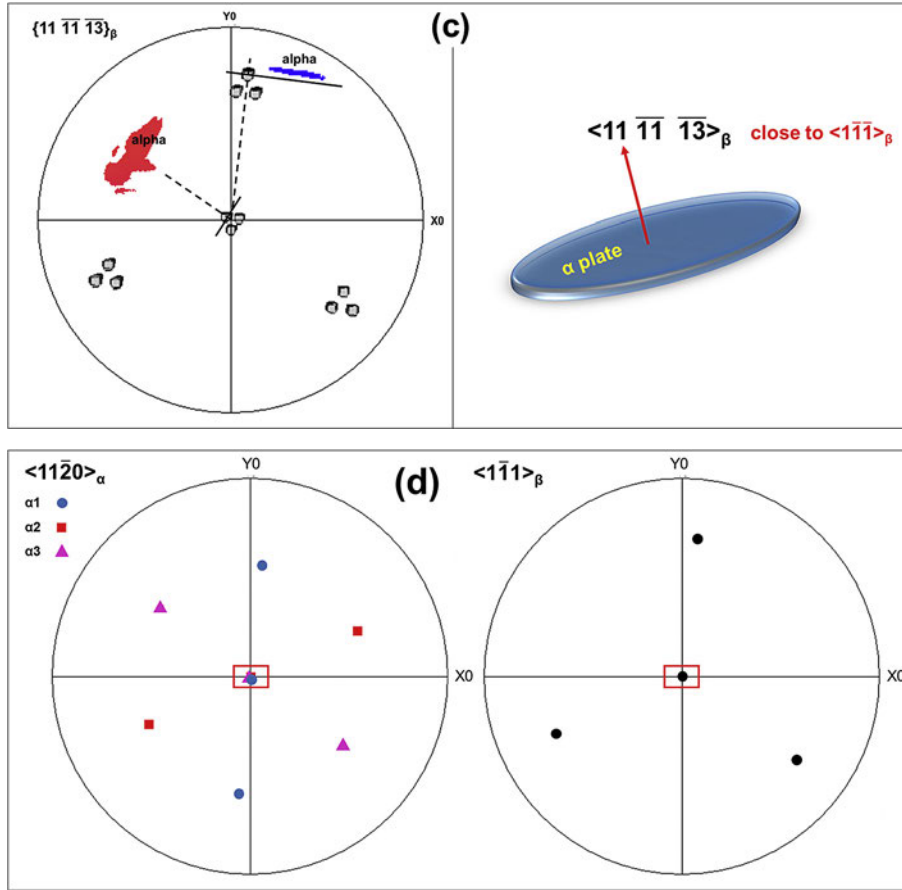


Fig. 4. (Continued).

oriented with their broad faces (the habit planes) almost parallel to the sample surface and the other variants oriented with their broad faces roughly perpendicular to the sample surface, as illustrated with the EBSD micrographs of two example  $\alpha$  plates in Fig. 4(c). With the two 2D sections of the  $\alpha$  precipitates, the 3D morphology can be obtained, as illustrated in Fig. 4(c). They are in plate shape, as reported in the literature, but the shape of the plate is not regular, as shown in Fig. 4(a). The thickness direction of the plate is  $\langle 11 \bar{1} 1 \bar{1} 3 \rangle_{\beta}$  close to  $\langle 1 \bar{1} 1 \rangle_{\beta}$ , as shown in Fig. 4(c).

Global orientation analysis of intragranular  $\alpha$  precipitates demonstrated that no variant is privileged. Every potential BOR variant has a chance to form during the transformation. However, locally the  $\alpha$  plates are organized into a triangular structure with 3 variants each forming one edge of the triangle, as outlined with the black rectangle in Fig. 4(a). Such a characteristic pattern of intragranular  $\alpha$  is also typical for metastable  $\beta$  Ti alloys [20]. The 3 variants possess specific orientation relationships. They share one common  $\langle 11 \bar{2} 0 \rangle_{\alpha}$  axis that is also the BOR direction of the surrounding  $\beta$  phase and are interrelated by a  $60^\circ$  rotation around the common  $\langle 11 \bar{2} 0 \rangle_{\alpha}$  axis, as shown in Fig. 4(d). This demonstrates that locally variant selection does occur during the transformation. It has been revealed that such an organization results from the accommodation of transformation strain of one variant by the others [38,39].

#### 3.4. Sub structures of intragranular $\alpha$ precipitates

To investigate the structure details within intragranular  $\alpha$  plates and their crystallographic characteristics, we carried out TEM

examinations. In general, the diffraction contrast of  $\alpha$  plates is not constant with large variations, indicating that the lattice of  $\alpha$  plates is not perfect but highly defected. However, no dislocation lines can be clearly seen within the  $\alpha$  plates by tilting the sample. In contrast, large amount of Moiré fringes can be revealed by the TEM diffraction contrast at certain sample tilts, as shown by the bright and dark field images in Fig. 5(a). These fringes arise from lattice misfits in the thickness direction of the foil. The fringes are oriented in several directions. This indicates that they are either from angular lattice misfits in a monocrystalline or from domains with different crystallographic orientations and infers that the  $\alpha$  lattice is highly strained. Furthermore, large amount of dislocation arrays are observed in the surrounding  $\beta$  matrix, as shown in Fig. 5(b), indicating the existence of lattice mismatch between the two phases.

Close examinations revealed that the  $\alpha$  plates are not monocrystalline. Each plate contains two different kinds of  $\alpha$  domains with different morphologies, different crystallographic orientations and at different sites with respect to the host  $\alpha$  plate. Hereafter we refer the host  $\alpha$  plate as major  $\alpha$ .

The first kind of  $\alpha$  domains are in particle shape with sizes of about 20 nm and situated at the surface of the major  $\alpha$  plate, as shown in Fig. 6(a) and (b) where the  $\alpha$  plates are presented with their broad faces oriented in two specific orientations, one being parallel to the TEM screen and the other perpendicular to the screen. These two specific orientations of the major  $\alpha$  plate allow resolving the 3D morphology of the  $\alpha$  domains and their sites and sizes. We denote such  $\alpha$  domains interface  $\alpha$ . Further crystallographic orientation analyses using Selected Area Electron Diffraction (SAED) pattern of all the  $\alpha$  domains attached to one major  $\alpha$

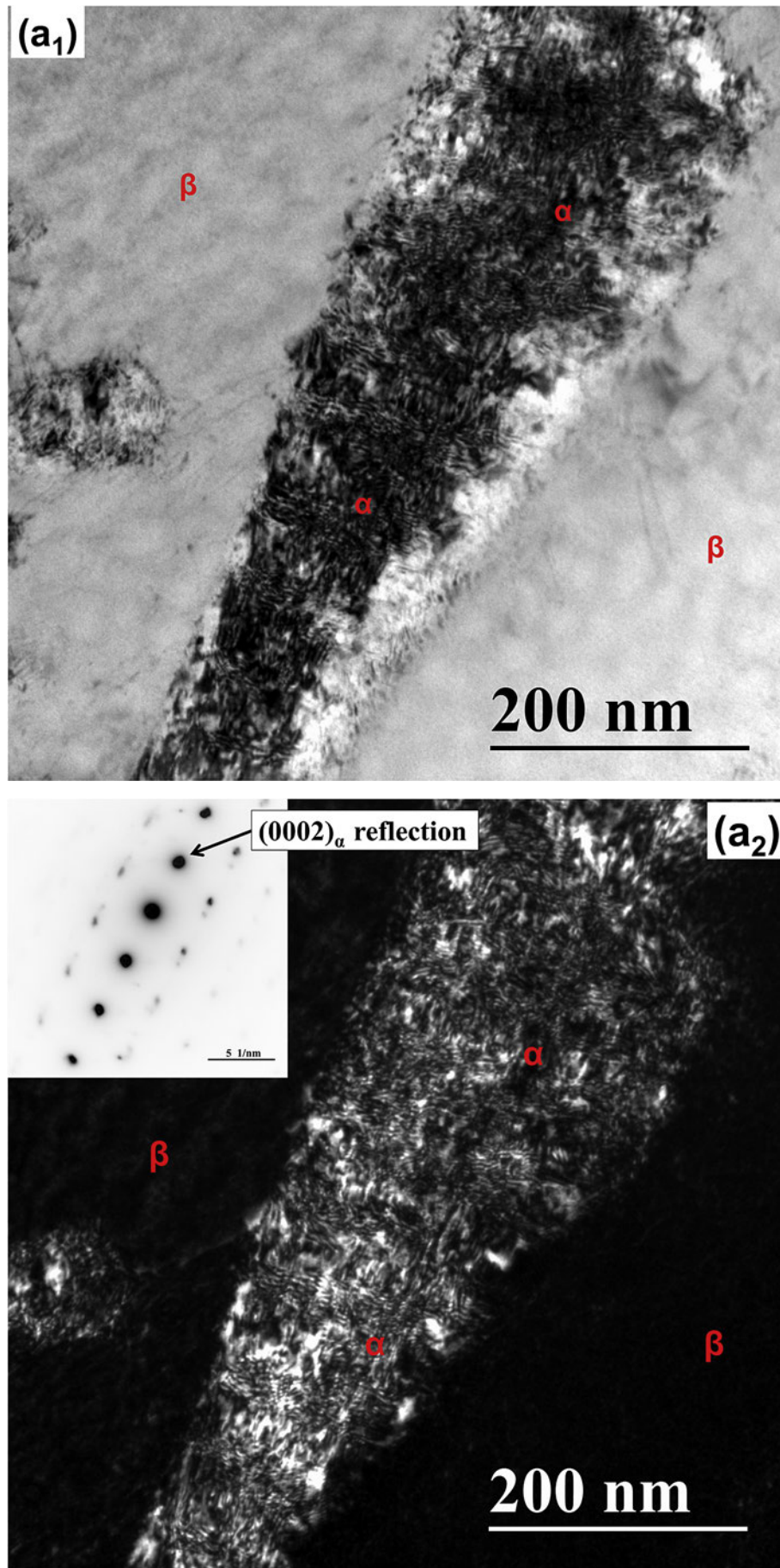


**Fig. 5.** (a<sub>1</sub>) and (a<sub>2</sub>) TEM bright field and dark field images of  $\alpha$  plate showing differently oriented Moiré fringes arising from lattice misfits. The dark field image is obtained using the  $\alpha$   $(0002)_\alpha$  reflection indicated in (a<sub>2</sub>). (b) TEM bright field image showing dislocation arrays stretching from  $\alpha/\beta$  interfaces.

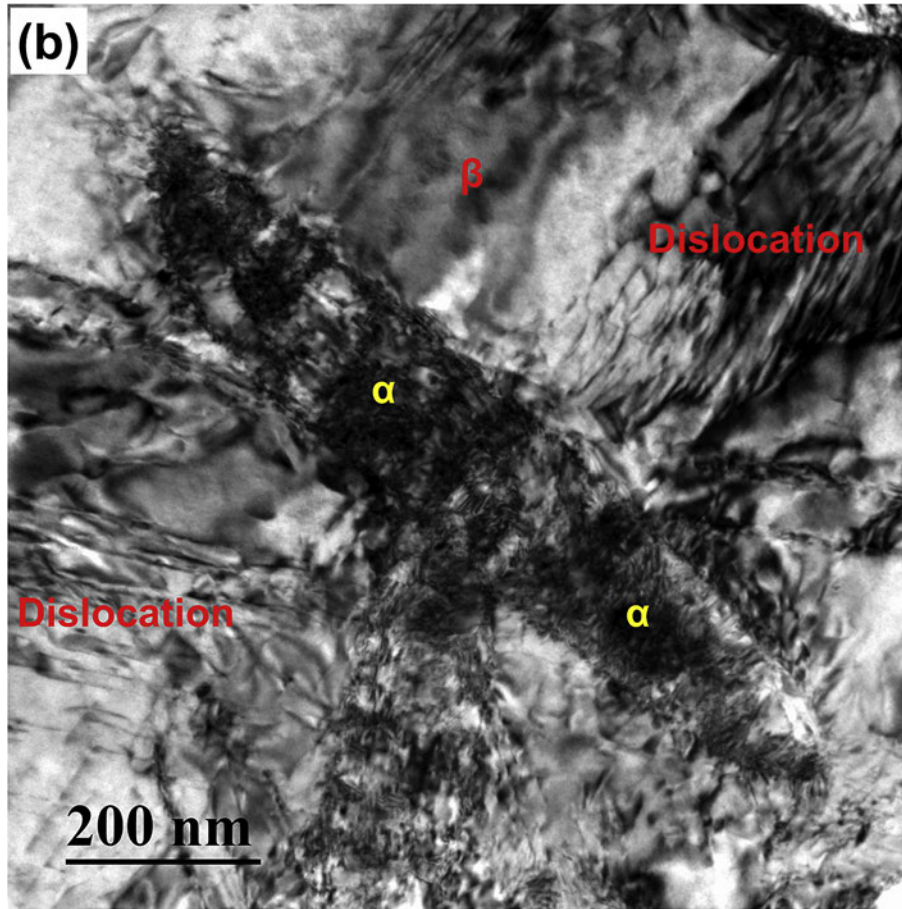


Fig. 5. (Continued).

plate, as shown in Fig. 7(a), revealed that these  $\alpha$  domains possess one crystallographic orientation, as shown by the SAED pattern in Fig. 7(a). The orientation relationships between the interface  $\alpha$  and the  $\beta$  matrix and the major  $\alpha$  are further calculated using their orientations determined by indexing the acquired Kikuchi line patterns, as shown in Fig. 7(b). Results show that these domains possess the BOR with the adjacent  $\beta$  matrix and are related with the major  $\alpha$  plate by a  $60^\circ$  rotation around the  $\langle 11\bar{2}0 \rangle_\alpha$  axis, as shown by the pole figures in Fig. 7(c). The interface  $\alpha$  has the same orientation as that of one neighboring major  $\alpha$  plate that forms the triangular structure. Such kind of  $\alpha$  domains has been theoretically predicted by the 3D phase field simulations, using Ti 6Al 4V [21]. According to [21], their formation is induced by the stress field of the major  $\alpha$  plate. The present results offer an experimental evidence for the simulated result. It should be noted that the materials used in Ref. [21] and in the present work are different in composition. However the characteristics concerning the interface  $\alpha$  domains are the same. This infers that the formation of such  $\alpha$  domains is a common feature of Al containing metastable  $\beta$  Ti alloys.

The second type of  $\alpha$  domains are in plate shape with a thickness of about 20 nm and run through the major  $\alpha$  plates, as shown in Fig. 8(a<sub>1</sub>). We denote such  $\alpha$  domains penetrating  $\alpha$ . Different from the interface  $\alpha$ , the penetrating  $\alpha$  lamellae are organized in parallel bands and the bands are repeated regularly, as seen in Fig. 8(a<sub>2</sub>). In each band, the penetrating  $\alpha$  domains are aligned and spaced regularly, as illustrated in Fig. 8(b). Further orientation analysis using the SAED and the Kikuchi pattern of

the penetrating  $\alpha$  domains, the major  $\alpha$  plate and the  $\beta$  matrix revealed that the broad face of the bands are roughly normal to the  $\langle 11\bar{2}0 \rangle_\alpha$  of the major  $\alpha$  plate or the  $\langle \bar{1}1\bar{1} \rangle$  of the  $\beta$  matrix, as illustrated in Fig. 8(b). Analysis with the SAED patterns obtained from the penetrating  $\alpha$  domains within one major  $\alpha$  plate demonstrated that they possess the same orientation, as shown by the SAED patterns in Fig. 9(a). Calculations using the orientations determined from the Kikuchi patterns of the penetrating  $\alpha$ , the major  $\alpha$  and the surrounding  $\beta$  matrix, as shown in Fig. 9(b), showed that the penetrating  $\alpha$  is related to the major  $\alpha$  by a  $60^\circ$  around the  $\langle 11\bar{2}0 \rangle_\alpha$  axis but it does not obey the BOR with the  $\beta$  matrix, as shown with the pole figures in Fig. 9(c). Such  $\alpha$  domains has not been reported in the literature, thus the origin of their formation is not yet known.

For the  $\beta$  matrix around each major  $\alpha$  plate, large amount of dislocations are present. The dislocations are organized in parallel arrays, as shown in Fig. 10. The lines stretch from the  $\alpha/\beta$  interfaces to the interior of the  $\beta$  matrix. Further analysis using the determination method in Ref. [30] demonstrated that they are mainly  $\langle \bar{1}\bar{1}1 \rangle \{110\}_\beta$  edge dislocations that are typical of BCC metals.

## 4. Discussion

### 4.1. Transformation strain characters

For the  $\beta$  to  $\alpha$  transformation in Ti alloys, in addition to the diffusion process, it evolves a structure change from the BCC to HCP system through lattice deformation, like the case of martensitic

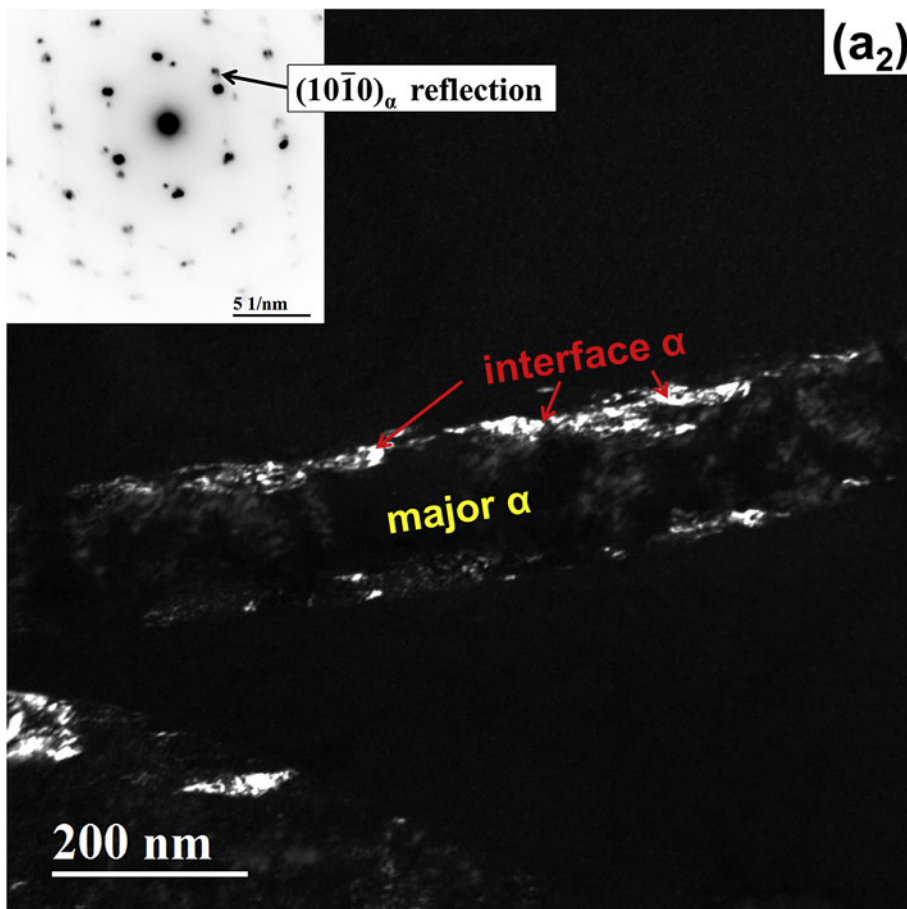
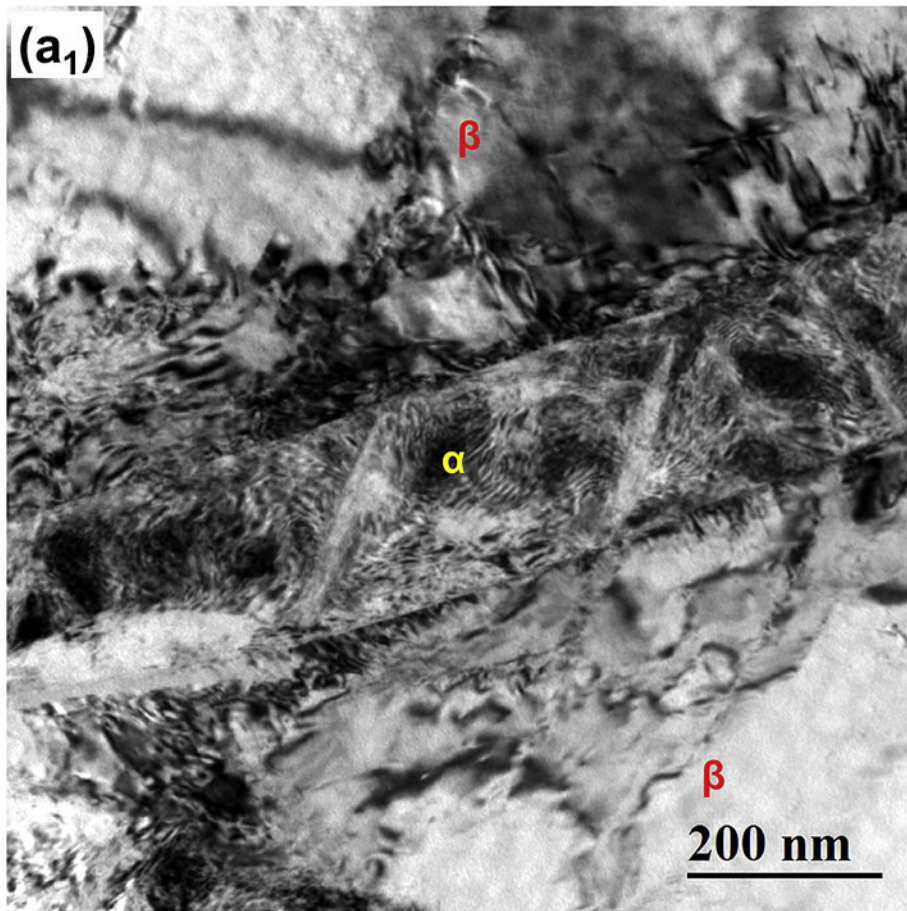


**Fig. 6.** TEM bright and dark field images of two differently oriented major  $\alpha$  plates showing the  $\alpha$  domains situated on the surface of these plates. (a<sub>1</sub>) and (a<sub>2</sub>) the major  $\alpha$  plate is with its habit plane perpendicular to the TEM screen. The dark field image is obtained using the  $(10\bar{1}0)_\alpha$  reflection indicated in (a<sub>2</sub>). (b<sub>1</sub>) and (b<sub>2</sub>) the major  $\alpha$  plate is with its habit plane parallel to the TEM screen. The dark field image is obtained using the  $(10\bar{1}0)_\alpha$  reflection indicated in (b<sub>2</sub>).

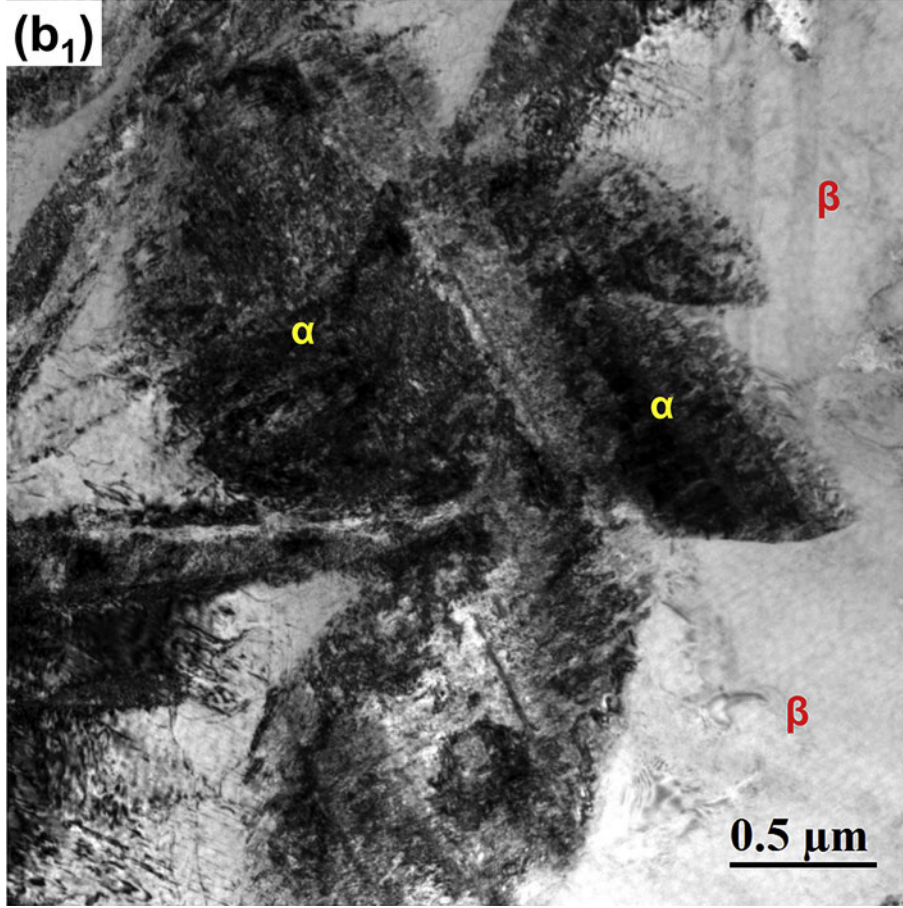


Fig. 6. (Continued).

transformation. By examining the atomic correspondences between the two phases, the deformation gradient tensor for the structure transformation in the stress free condition can be obtained. For the present transformation, the BOR is obeyed by the two phases, thus the deformation gradient tensor  $\mathbf{A}$  [40] expressed in the frame of the BOR, as shown in Fig. 11, can be established. As displayed in Eq. (1),  $a_{ii}$  ( $i = 1, 2$  and  $3$ ), the diagonal elements, means elongation ( $a_{ii} > 1$ ) or contraction ( $a_{ii} < 1$ ) in the  $i$  direction, whereas  $a_{ij}$  ( $i$  and  $j = 1, 2$  and  $3$ ), the off diagonal elements, means a shear in the direction of  $i$  and on the plane normal to  $j$ . The normal strain is accumulative in  $i$ , whereas the shear amount is proportional to the dimension in the direction normal to the shear plane, i.e. in  $j$ . This means that the normal strain restricts the growth of the new phase in the strain direction, whereas the shear strain confines the growth of the new phase in the direction normal to the shear plane.

$$\mathbf{A} = \begin{bmatrix} a_{11} & a_{12} & a_{13} \\ a_{21} & a_{22} & a_{23} \\ a_{31} & a_{32} & a_{33} \end{bmatrix} \quad (1)$$

For the present alloy, the deformation gradient tensor of the variant satisfying  $(110)_\beta // (0001)_\alpha$  and  $[\bar{1}\bar{1}\bar{1}]_\beta // [11\bar{2}0]_\alpha$  is given in Table 2 in the BOR reference frame (as shown in Fig. 11). It is seen that the formation of this variant requires a contraction of 0.0416 in the  $[\bar{1}\bar{1}\bar{2}]_\beta$  direction ( $a_{11}$ ), an elongation of 0.0434 in the  $[\bar{1}\bar{1}\bar{1}]_\beta$   $a_{22}$ , an elongation of 0.0189 in the  $[110]_\beta$  direction  $a_{33}$  and a shear of 0.1844 on the  $(\bar{1}\bar{1}\bar{2})_\beta$  plane and in the  $[\bar{1}\bar{1}\bar{1}]_\beta$  direction  $a_{21}$ , as summarized in Table 3. It is seen that the most important strain is

the shear on the plane of  $(\bar{1}\bar{1}\bar{2})_\beta$  and in the  $[\bar{1}\bar{1}\bar{1}]_\beta$  direction that is more than 3 times higher than that of the contraction in the  $[\bar{1}\bar{1}\bar{2}]_\beta$  direction and the elongation in the  $[\bar{1}\bar{1}\bar{1}]_\beta$  direction and almost one order higher than the elongation in the  $[110]_\beta$  direction.

Such a deformation characterized by a large shear strain well explains the plate shape of the major  $\alpha$ . One can find that the orientation of the plane of the  $[\bar{1}\bar{1}\bar{1}]_\beta / (\bar{1}\bar{1}\bar{2})_\beta$  shear ( $a_{21}$ ) is close to that of the habit plane  $(11\bar{1}\bar{1}\bar{3})_\beta$  (with an angular deviation of about  $15^\circ$ ) that is also the broad face of the  $\alpha$  phase. Thus this shear restricts the thickening of the  $\alpha$  precipitate in the direction perpendicular to the habit plane during the growth process. Moreover, the normal strain component  $a_{11}$  also restricts the growth of the  $\alpha$  precipitate in this direction. Finally, the precipitated  $\alpha$  develops into plate shape. The dimension of the  $\alpha$  precipitates in the direction normal to the  $(11\bar{1}\bar{1}\bar{3})_\beta$  is indeed the smallest, as is evidenced for the major  $\alpha$  plates in the present alloy.

#### 4.2. Formation of interface $\alpha$ and local variant selection of major $\alpha$

With the determined orientation of the interface  $\alpha$  with respect to the major  $\alpha$  plate ( $60^\circ / \langle 11\bar{2}0 \rangle_\alpha$ ) and the surrounding  $\beta$  matrix (BOR), the deformation gradient tensors of such  $\alpha$  variants were calculated and expressed in the BOR frame of the major  $\alpha$  plate. The tensors are displayed in Table 4. For reference, the deformation gradient tensors of the other BOR variants were also calculated in the frame of the major  $\alpha$  plate and displayed in Table 4. It is seen that among all the 11 possible BOR  $\alpha$  variants, only the V1 and V2

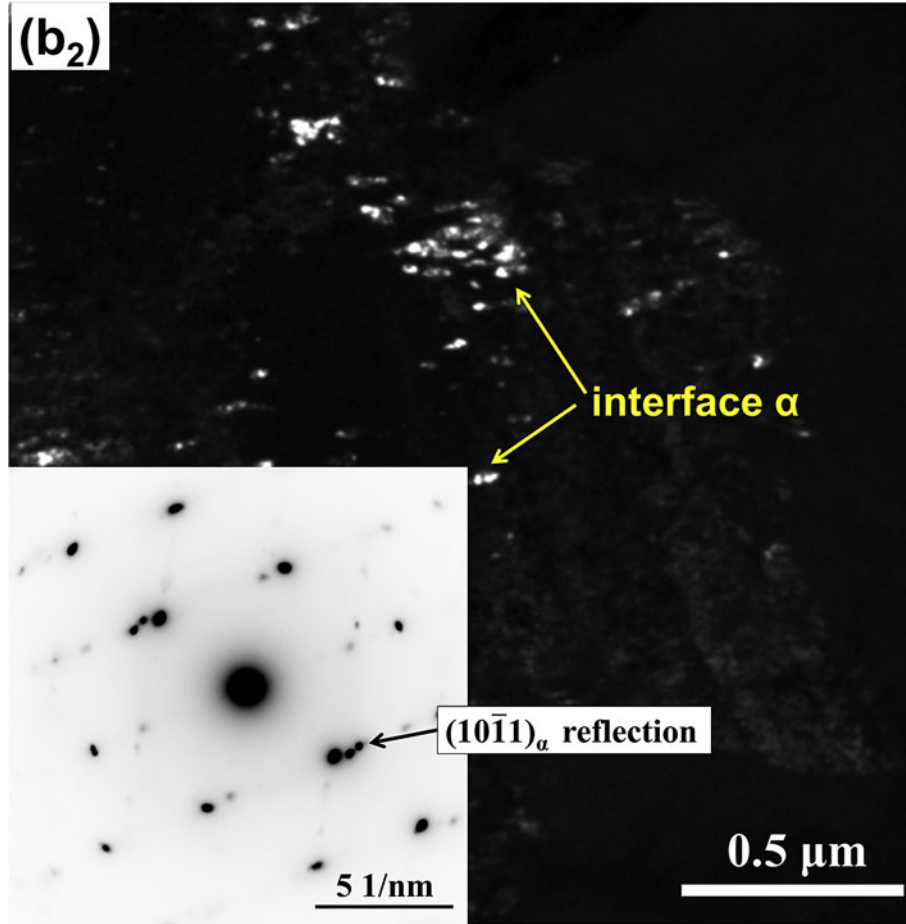


Fig. 6. (Continued).

that are related with the major  $\alpha$  plate by a  $60^\circ/\langle 11\bar{2}0 \rangle_\alpha$  rotation have the highest positive  $a_{21}$ . That means that these variants have the highest accommodation capacity for the shear deformation generated by the major  $\alpha$  variant. In addition, the  $a_{11}$  of these variants is larger than 1 (elongation), thus they can well accommodate the lattice contraction of the major  $\alpha$  plate in this direction ( $a_{11}$  of the major  $\alpha$  plate is smaller than 1). As analyzed above, for these two components ( $a_{21}$  and  $a_{11}$ ), the highest deformation happens at the surface of the major  $\alpha$  plate. This is the exact place where are the interface  $\alpha$  domains in the present alloy. Thus the formation of the interface  $\alpha$  domains is indeed induced by the local deformation generated by the major  $\alpha$  plate. Moreover, the values of  $a_{i2}$  of the two variants (V1 and V2) (Table 4) are exactly the same as those of the major  $\alpha$  plate (Table 2), meaning that the growth of the interface  $\alpha$  in the direction of  $[\bar{1}\bar{1}\bar{1}]_\beta$  is totally compatible with the major  $\alpha$  plate. However, the values of  $e_{i3}$  of the interface  $\alpha$  are quite different from the corresponding values of the  $a_{i3}$  of the major  $\alpha$ , thus the growths of the two kinds of  $\alpha$  in the direction of  $[110]_\beta$  are not compatible. This may be one of the reasons that the interface  $\alpha$  domains are in particle shape. Another reason may be the incompatible interface between the two  $\alpha$ .

From Table 4 one can find that variants V4 and V10 also possess accommodation capacity to the shear deformation generated by the major  $\alpha$  plate (the  $a_{21}$  is positive and the second largest among the 11 variants). The appearance of these variants has been predicted by the theoretical simulation [21]. However, in the present work, we did not find their existence. This may be due to their poor

geometrical compatibility with the major  $\alpha$  plate in the directions of  $[\bar{1}\bar{1}\bar{1}]_\beta$  and  $[110]_\beta$ . It is seen from Table 4 that their values of  $a_{2i}$  and  $a_{3i}$  are very different from those of the corresponding  $a_{2i}$  and  $a_{3i}$  of the major  $\alpha$ , especially  $a_{22}$ . The  $a_{22}$  of V4 and V10 are smaller than 1, meaning contraction, whereas that of the major  $\alpha$  plate is larger than 1, meaning elongation. Thus in the direction of  $[\bar{1}\bar{1}\bar{1}]_\beta$ , the growth of the two  $\alpha$  is totally incompatible. Therefore, compared with variants V1 and V2, variants V4 and V10 are less favorable. They may form under very specific local strain conditions but their occurrence is certainly minor. This corresponds to our experimental observation.

It should be noted from Table 4 that the formation of the interface  $\alpha$  can only accommodate one part of the shear strain at the broad faces of the major  $\alpha$  plate. Moreover it also generates a relative large shear  $a_{23}$  (0.1597). Thus the remaining part of the shear  $a_{21}$  from the major  $\alpha$  plate and the newly created shear  $a_{23}$  from the interface  $\alpha$  should be accommodated by other mechanical systems of either the major  $\alpha$  plate or the surrounding  $\beta$  matrix. Further analysis shows that the shear system of  $a_{21}$  is in coincidence with the  $\{\bar{1}12\} \langle 1\bar{1}\bar{1} \rangle_\beta$  slip system of the surrounding  $\beta$  matrix. This slip system is also in geometrical consistent with one of the prismatic slip  $\{0002\} \langle 11\bar{2}0 \rangle_\alpha$  of the major  $\alpha$  plate. The shear system of  $a_{23}$  is in coincidence with the  $\{110\} \langle 1\bar{1}\bar{1} \rangle_\beta$  slip system. Our TEM examination on dislocations in  $\beta$  matrix did not reveal the existence of  $\{\bar{1}12\} \langle 1\bar{1}\bar{1} \rangle_\beta$  type dislocations in the  $\beta$  matrix near the major  $\alpha$  plate. However, large amount of Moiré fringes were observed in the major  $\alpha$  plate, as shown in Fig. 5(a), indicating the shear of  $a_{21}$  of the

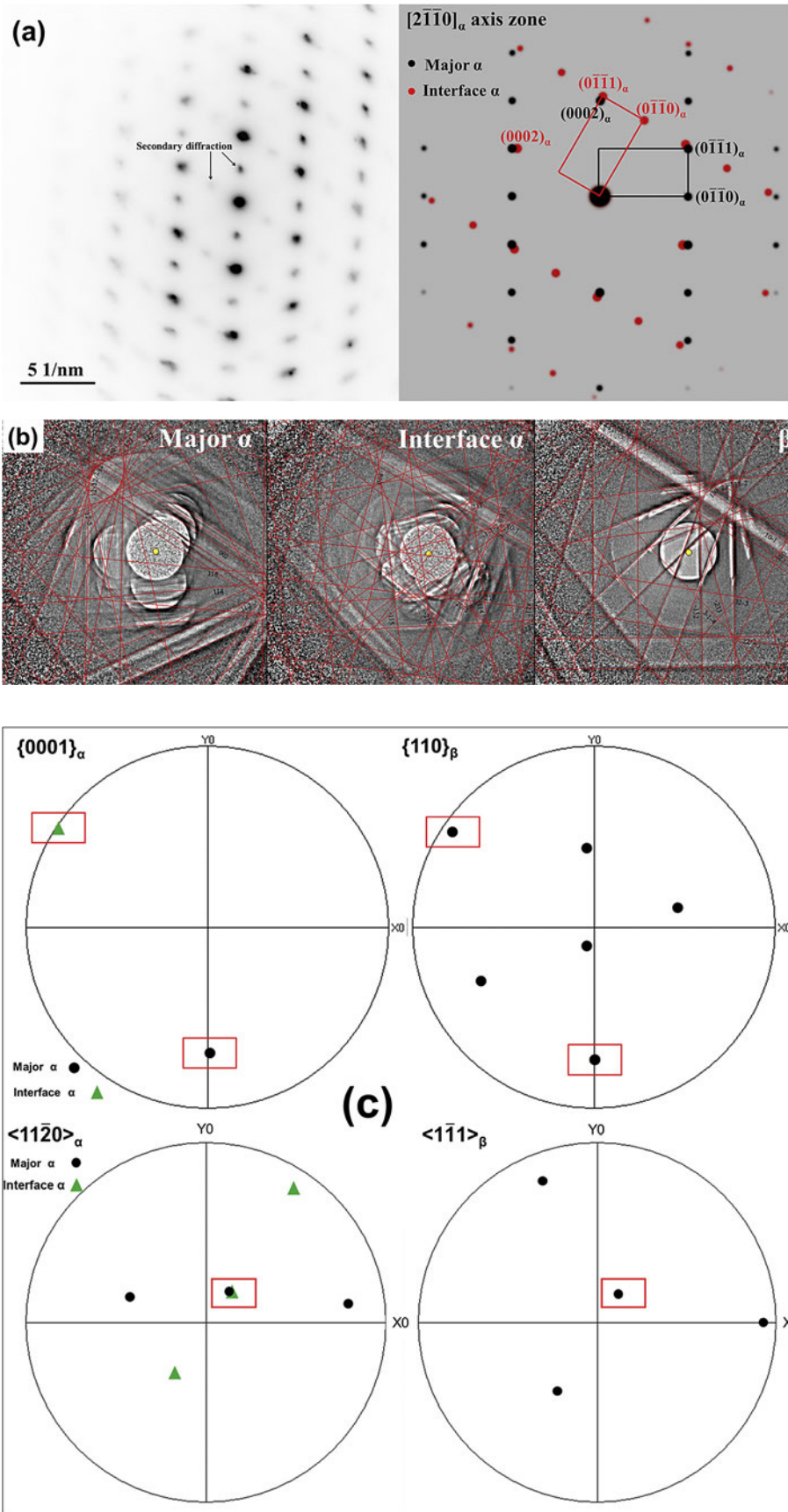


**Fig. 7.** (a) Selected Area Electron Diffraction (SAED) pattern of the interface  $\alpha$  domains attached to one major  $\alpha$  plate and the corresponding SAED pattern simulated using the Crystal Maker software. (b) TEM Kikuchi line patterns from the major  $\alpha$  plate, its interface  $\alpha$  domains and the surrounding  $\beta$  matrix. The red lines are the simulated Kikuchi lines using EP. (c) BOR plane and direction pole figures of the major  $\alpha$  plate, the interface  $\alpha$  domains and the surrounding  $\beta$  matrix. The common directions shared by the major  $\alpha$ , the interface  $\alpha$  and  $\beta$  matrix are outlined with the red rectangles. (For interpretation of the references to colour in this figure legend, the reader is referred to the web version of this article.)

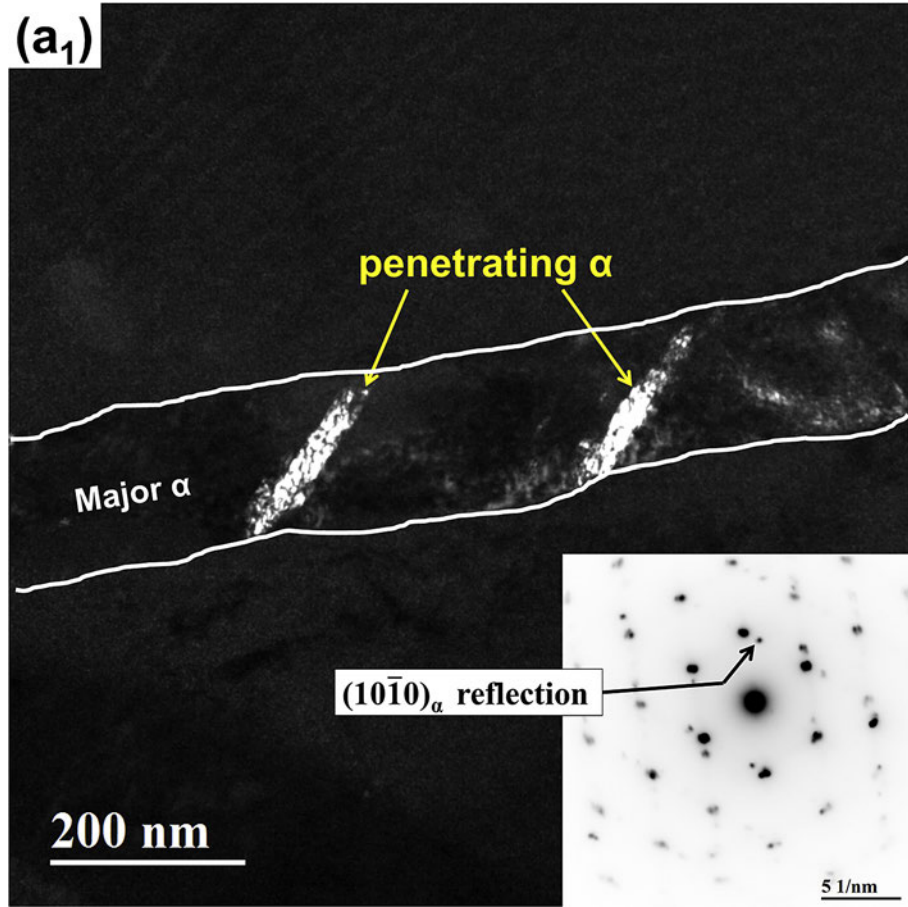


**Fig. 8.** TEM dark field images of two differently oriented major  $\alpha$  plates showing the penetrating  $\alpha$  domains in the major  $\alpha$  plate and the illustration of the band of the penetrating  $\alpha$  domains. **(a<sub>1</sub>)** and **(a<sub>2</sub>)** the major  $\alpha$  plate is with its habit plane perpendicular and parallel to the TEM screen. The dark field image is obtained using the  $(10\bar{1}0)_\alpha$  and the  $(0\bar{1}10)_\alpha$  reflection, respectively. **(b)** Illustration of the band of penetrating  $\alpha$  band in the major  $\alpha$  plate.

major  $\alpha$  plate may be absorbed mainly by its prismatic slip [41,42], as it is well known that the prismatic slip of the  $\alpha$  phase of the Ti has very small critical resolved shear stress (CRSS) [43,44]. The activation of the prismatic slip may be much easier than the activation of the  $\{\bar{1}12\}\langle 1\bar{1}1\rangle_\beta$  slip of the  $\beta$  phase. For the shear of  $a_{23}$ , our TEM examination did evidence the existence of  $\{110\}\langle 1\bar{1}1\rangle_\beta$  dislocations in the form of arrays stretching from the interface of the major  $\alpha$  plate to the interior of the surrounding  $\beta$  matrix, as shown in Fig. 10. This indicates that the relative large value of the  $a_{23}$  resulting from the formation of the interface  $\alpha$  particles should be accommodated by the formation of the  $\{110\}\langle 1\bar{1}1\rangle_\beta$  dislocations in the nearby  $\beta$  matrix.

Obviously the interface  $\alpha$  particles further serve as sympathetic nuclei for the formation of the neighboring major  $\alpha$  plate with the same orientation and eventually contribute to formation of the triangular variant cluster of three  $60^\circ/[11\bar{2}0]_\alpha$  inter related major  $\alpha$  plates, as shown in Fig. 4(a). Thus the formation of each triangular variant cluster is to minimize the shear strain generated by the major  $\alpha$  plates in the cluster. Moreover, by obeying the BOR, the low CRSS shear systems of the major  $\alpha$  plates (the prismatic slip) and the  $\beta$  matrix ( $\{110\}\langle 1\bar{1}1\rangle_\beta$ ) are in perfect geometrical consistency with the lattice deformation components of the structure transformation. The transformation strains can be further accommodated by the activation of these compatible systems, thus the formation of the triangular clusters is energetically favorable in terms of minimizing the overall transformation strain.

#### 4.3. Formation of non BOR $\alpha$ domains (penetrating $\alpha$ )

The above analysis shows that by forming the interface  $\alpha$  and the triangular  $\alpha$  cluster, the shear deformation created by the displacive structure transformation from the  $\beta$  phase to the major  $\alpha$  plates can be well accommodated. However, the normal strain, especially  $a_{22}$  (Table 2), of each major  $\alpha$  plate is not accommodated. This strain becomes unignorable when the major  $\alpha$  plate enlarges its dimension in the  $[\bar{1}\bar{1}\bar{1}]_\beta$  direction. From Table 2 one can see that the value of  $a_{22}$  of the major  $\alpha$  plate is larger than 1, meaning that the  $\beta$  lattice extends in the  $[\bar{1}\bar{1}\bar{1}]_\beta$  direction when it transforms to the  $\alpha$  lattice and the remaining  $\beta$  lattice in the transformation front is contracted. The contraction accumulated with the growth of the major  $\alpha$  plate in this direction. Thus accommodation to release the constraint is needed. The formation of the penetrating  $\alpha$  bands that go through and are with their broad faces normal to the  $[\bar{1}\bar{1}\bar{1}]_\beta$  direction, as shown in Fig. 8(a) and (b) should be related to such a need.

To validate such a hypothesis, we established deformation gradient tensor of the penetrating  $\alpha$  and express it in the same BOR reference frame as their host major  $\alpha$  plate. With the determined BOR between the  $\beta$  matrix and the major  $\alpha$  ( $((110)_\beta//((0001)_\alpha$  and  $[\bar{1}\bar{1}\bar{1}]_\beta//[11\bar{2}0]_\alpha$ ) and the  $60^\circ/[\bar{1}2\bar{1}0]_\alpha$  rotation between the major  $\alpha$  and the penetrating  $\alpha$ , as shown by the pole figure in Fig. 9(c), the atomic correspondences between the  $\beta$  matrix and the penetrating  $\alpha$  were established, as shown in Fig. 12. As seen from the figures, no

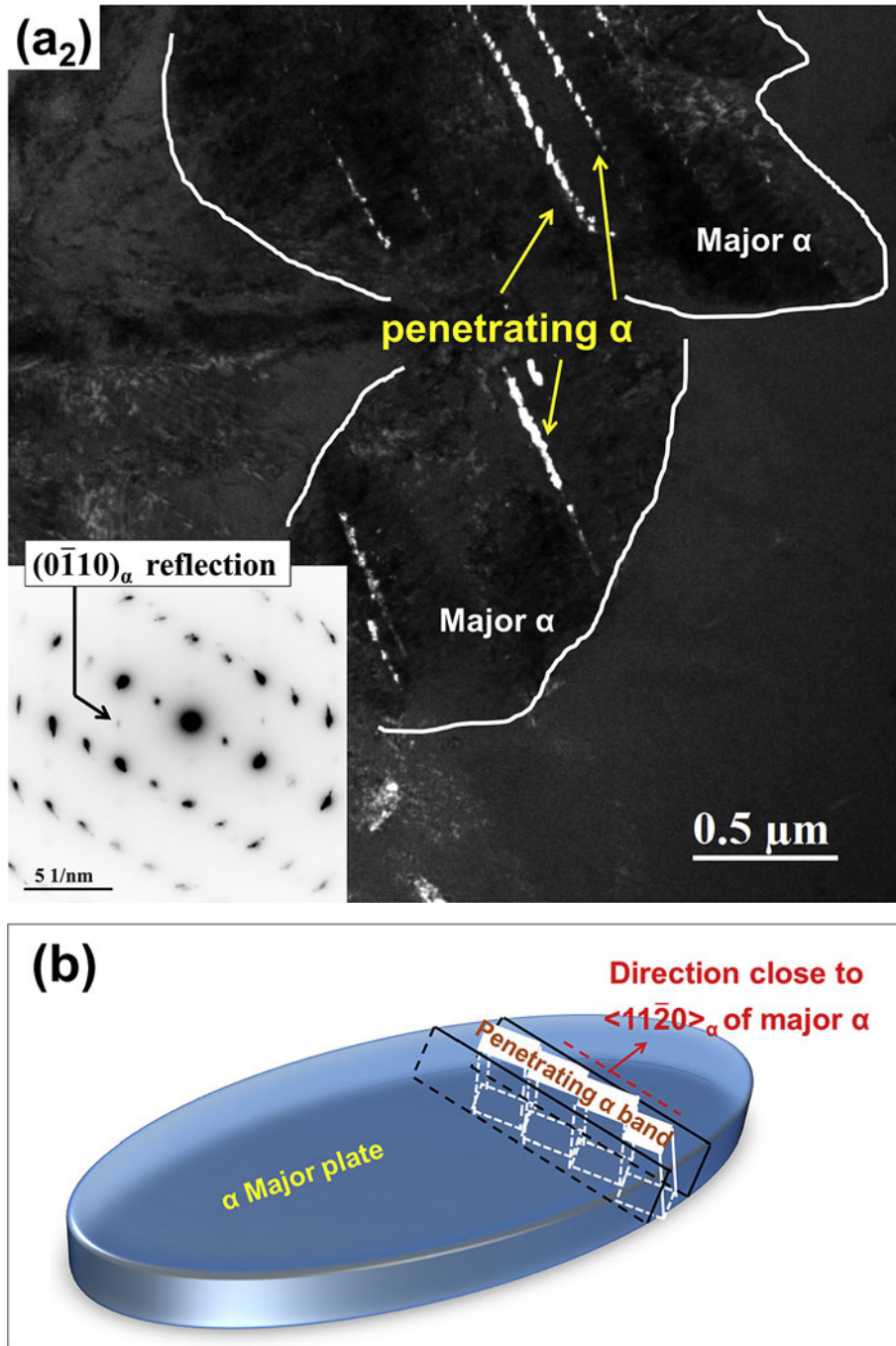
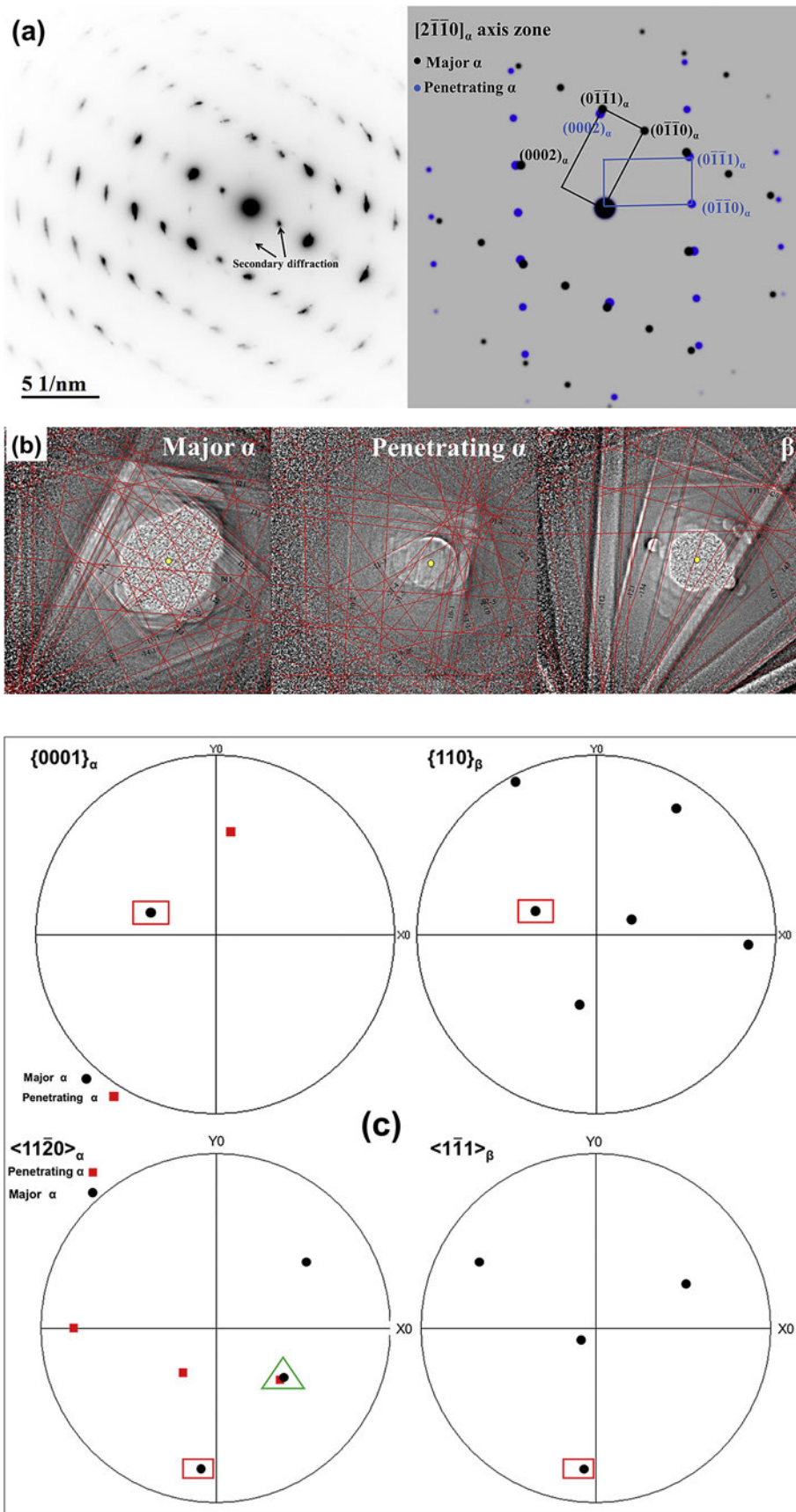


Fig. 8. (Continued).

plane and in plane direction parallelisms between the  $\beta$  phase and the penetrating  $\alpha$  can be figured out. This further demonstrates that the penetrating  $\alpha$  is transformed from the deformed  $\beta$ . By examining the atomic correspondences between the  $\beta$  and the penetrating  $\alpha$  via the major  $\alpha$ , we worked out the lattice deformation with the smallest atomic movements and thus obtained the deformation gradient tensor for the structure transformation of the  $\beta$  matrix to the penetrating  $\alpha$  plates expressed in the same BOR reference frame as for the major  $\alpha$  plate. The tensor is given in Table 5. It is seen that the formation of the penetrating  $\alpha$  domains ( $a_{22} = 0.8675$ ) indeed accommodates the normal strain in  $[\bar{1}\bar{1}\bar{1}]_{\beta}$  direction produced by the major  $\alpha$  plate ( $a_{22} = 1.0434$ ). Moreover,

the  $a_{11}$  ( $0.8984 < 1$ ; contraction) and the  $a_{21}$  ( $-0.286$ ; negative) of the penetrating  $\alpha$  demonstrate similar characters to the  $a_{11}$  ( $0.9584 < 1$ ; contraction) and the  $a_{21}$  ( $-0.1844$ ; negative) of the major  $\alpha$  plate, i.e., contraction in the  $[1\bar{1}\bar{2}]_{\beta}$  direction and shear on  $(1\bar{1}\bar{2})_{\beta}$  plane along the  $[\bar{1}\bar{1}\bar{1}]_{\beta}$  direction. Thus in the  $[1\bar{1}\bar{2}]_{\beta}$  direction, the growths of the two  $\alpha$  are rather compatible than accommodative. This corresponds well to the going through feature of the penetrating  $\alpha$  in the major  $\alpha$  plate, as these strains produce maximum deformations at the broad face of the major  $\alpha$  plate but not in the volume. However, it should be noted that the formation of the penetrating  $\alpha$  also creates relative large shears on the  $(1\bar{1}\bar{2})_{\beta}$  plane in the  $[110]_{\beta}$  direction ( $a_{31}$ ), and on the  $([\bar{1}\bar{1}\bar{1}]_{\beta}$  plane in the



**Fig. 9.** (a) Selected Area Electron Diffraction (SAED) pattern of the penetrating  $\alpha$  domains attached to one major  $\alpha$  plate and the corresponding SAED pattern simulated using the Crystal Maker software. (b) TEM Kikuchi line patterns from the major  $\alpha$  plate, the penetrating  $\alpha$  domains and the surrounding  $\beta$  matrix. The red lines are the simulated Kikuchi lines using EP. (c) BOR plane and direction pole figures of the major  $\alpha$  plate, the penetrating  $\alpha$  domains and the surrounding  $\beta$  matrix. The common directions shared by the major  $\alpha$  and the penetrating  $\alpha$  are outlined with the green triangle, and the common plane and direction shared by the major  $\alpha$  plate and the  $\beta$  matrix are outlined with the red rectangles. (For interpretation of the references to colour in this figure legend, the reader is referred to the web version of this article.)

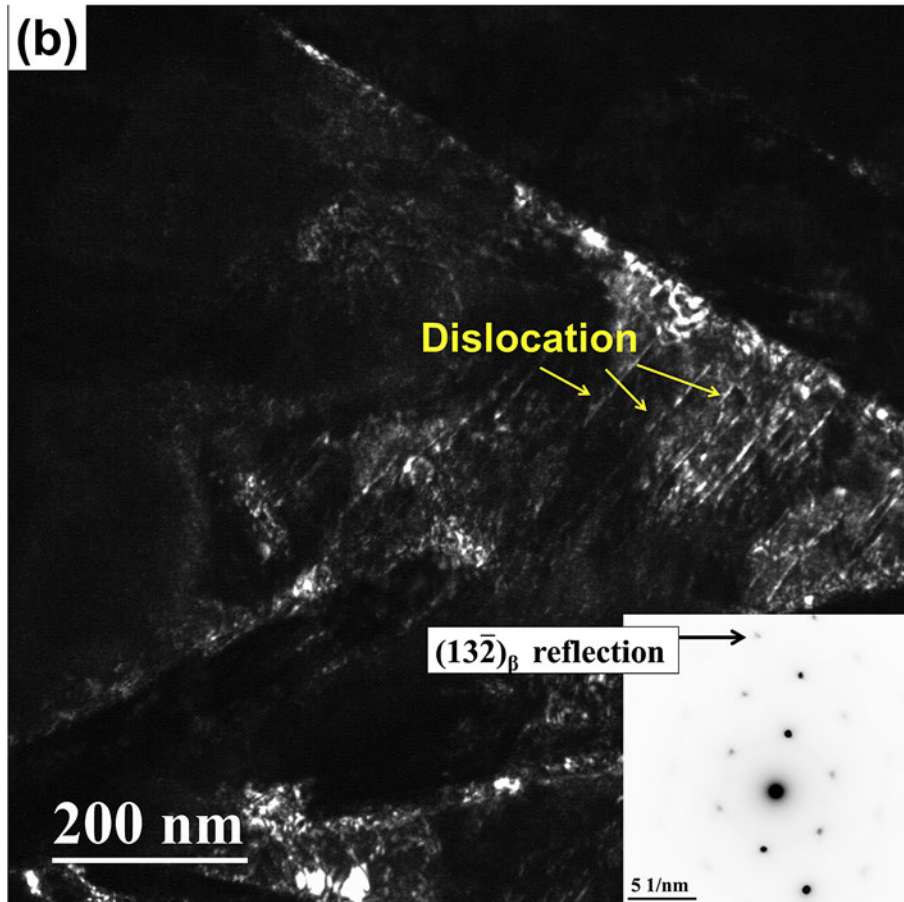
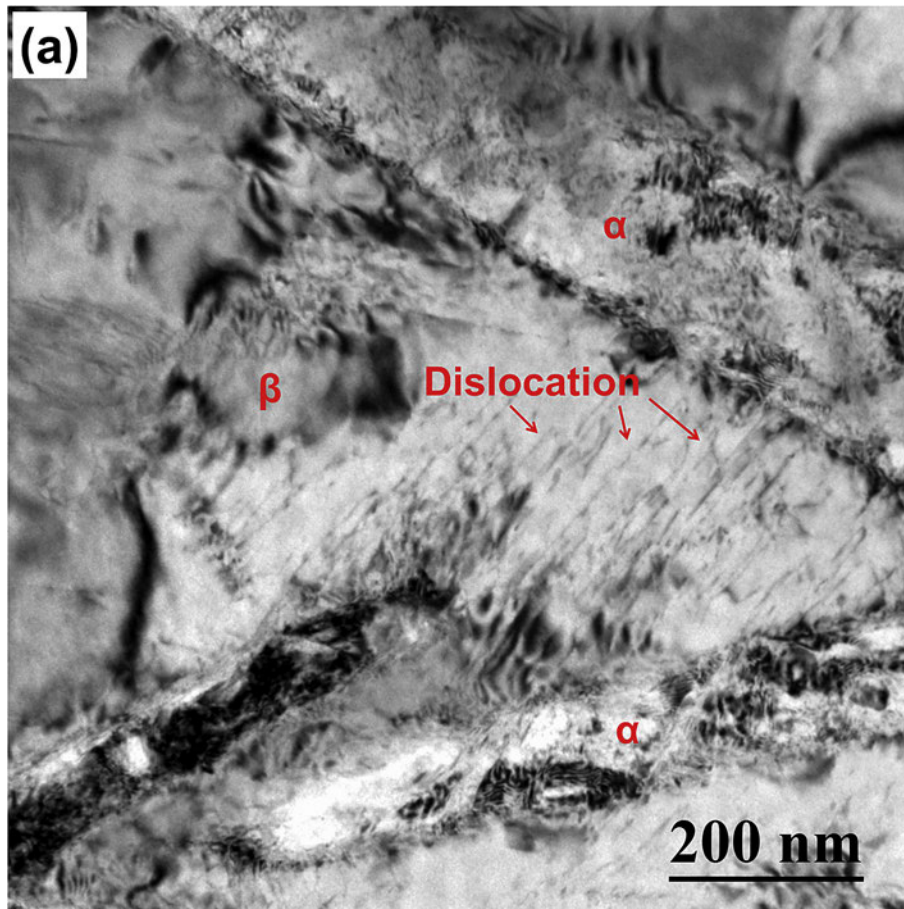
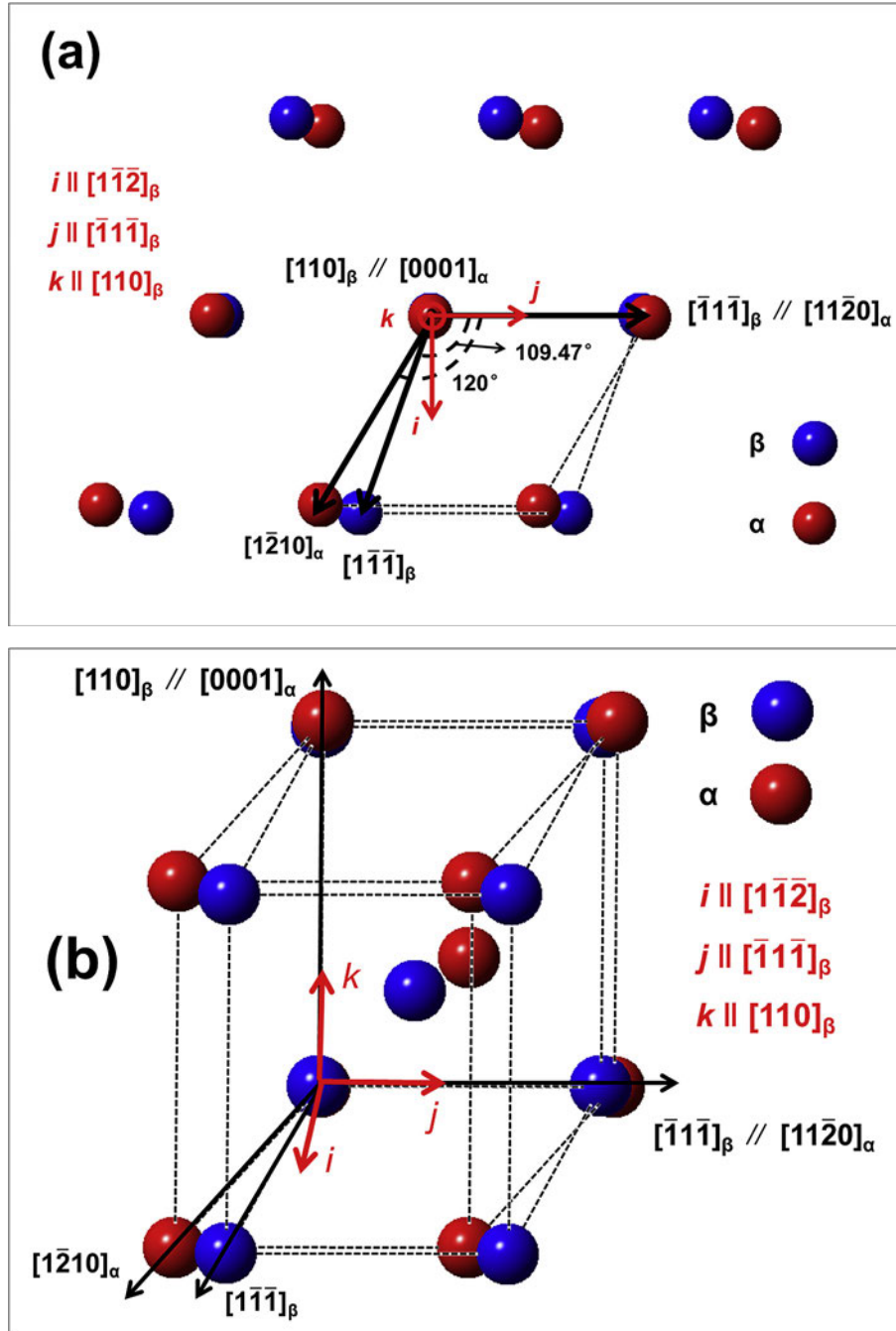


Fig. 10. (a) and (b) TEM bright field and dark field images showing dislocation arrays in  $\beta$  stretching from the  $\alpha/\beta$  interface. The dark field image is obtained using the  $(13\bar{2})_{\beta}$  reflection as indicated in the figure.



**Fig. 11.** (a) Atomic correspondences between  $\beta$  phase and  $\alpha$  phase on the BOR plane and the reference frame ( $i-j-k$ ) under the BOR, i.e.,  $j$  is parallel to the OR directions in the two phases,  $k$  to the direction normal to the OR planes in the two phases and  $i$  is the vector cross product of  $k$  and  $j$ . (b) 3D atomic correspondences between  $\beta$  phase and  $\alpha$  phase in the  $i-j-k$  reference frame.

$[110]_{\beta}$  direction ( $a_{32}$ ), especially the latter. However, for  $a_{31}$  and  $a_{32}$ , there are no slip systems or twinning systems in either  $\beta$  matrix or the major  $\alpha$  to accommodate these two shears. Thus the width of

the penetrating  $\alpha$  bands is very small due to the large restriction of  $a_{32}$ . Further accommodation of the  $a_{22}$  of the major  $\alpha$  during growth is realized by the repeated formation of the penetrating  $\alpha$  bands, as

**Table 2**  
Deformation gradient tensor of the variant expressed in its BOR reference frame ( $(110)_{\beta} \parallel (0001)_{\alpha}$  and  $[\bar{1}\bar{1}\bar{1}]_{\beta} \parallel [11\bar{2}0]_{\alpha}$ ).

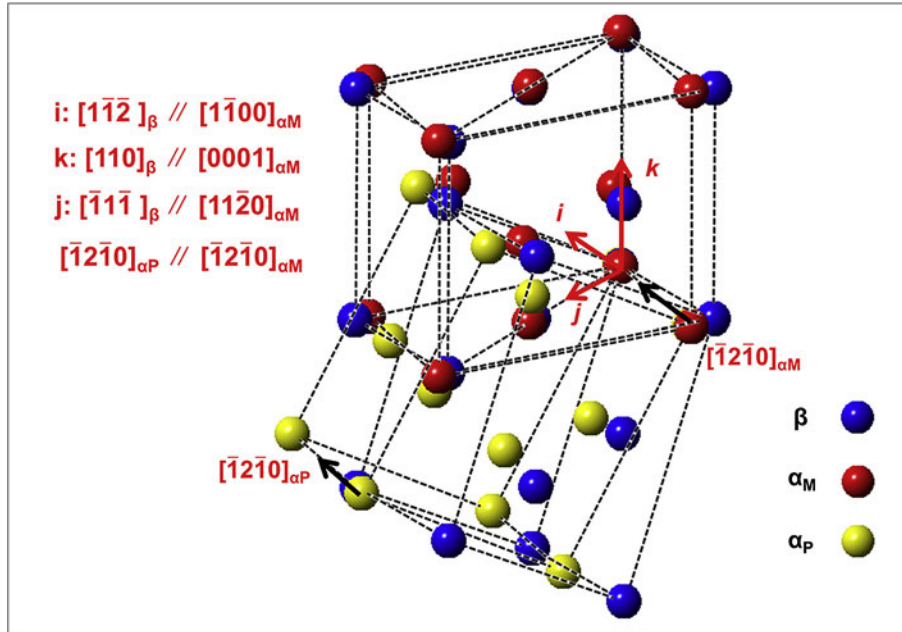
Variant	Deformation gradient tensor
$(110)_{\beta} \parallel (0001)_{\alpha}$	$\begin{bmatrix} 0.9584 & 0 & 0 \\ -0.1844 & 1.0434 & 0 \\ 0 & 0 & 1.0189 \end{bmatrix}$
$[\bar{1}\bar{1}\bar{1}]_{\beta} \parallel [11\bar{2}0]_{\alpha}$	

**Table 3**  
Strain components of the transformation deformation.

Deformation	Strain
Dilation $[1\bar{1}\bar{2}]_{\beta}$	0.0416
Dilation $[\bar{1}\bar{1}\bar{1}]_{\beta}$	0.0434
Dilation $[110]_{\beta}$	0.0189
Shear $(1\bar{1}\bar{2})[\bar{1}\bar{1}\bar{1}]_{\beta}$	0.1844

**Table 4**Deformation gradient tensors of the other 11 possible BOR  $\alpha$  variants expressed in the BOR frame of the major  $\alpha$  plate in Table 2 and the disorientation with it.

No.	Variant	Deformation gradient tensor	Disorientation
V1	$(10\bar{1})_{\beta} // (0001)_{\alpha}$ $[111]_{\beta} // [11\bar{2}0]_{\alpha}$	$\begin{bmatrix} 1.0038 & 0 & 0.0262 \\ 0.0922 & 1.0434 & -0.1597 \\ 0.0262 & 0 & 0.9735 \end{bmatrix}$	$60^{\circ} // (11\bar{2}0)$
V2	$(01\bar{1})_{\beta} // (0001)_{\alpha}$ $[\bar{1}\bar{1}\bar{1}]_{\beta} // [11\bar{2}0]_{\alpha}$	$\begin{bmatrix} 1.0038 & 0 & -0.0262 \\ 0.0922 & 1.0434 & 0.1597 \\ -0.0262 & 0 & 0.9735 \end{bmatrix}$	$60^{\circ} // (11\bar{2}0)$
V3	$(101)_{\beta} // (0001)_{\alpha}$ $[\bar{1}\bar{1}\bar{1}]_{\beta} // [11\bar{2}0]_{\alpha}$	$\begin{bmatrix} 1.0680 & 0.0695 & 0.1419 \\ -0.0277 & 0.9792 & -0.0780 \\ -0.0087 & -0.0247 & 0.9735 \end{bmatrix}$	$60.832^{\circ} // (\bar{1}.377 \bar{1} 2.377 0.359)$
V4	$(\bar{1}0\bar{1})_{\beta} // (0001)_{\alpha}$ $[\bar{1}\bar{1}\bar{1}]_{\beta} // [11\bar{2}0]_{\alpha}$	$\begin{bmatrix} 1.0548 & -0.0134 & -0.0011 \\ 0.0789 & 0.9792 & -0.0193 \\ 0.1495 & -0.0726 & 0.9867 \end{bmatrix}$	$63.2618^{\circ} // (\bar{1}0 5 5 \bar{3})$
V5	$(\bar{1}0\bar{1})_{\beta} // (0001)_{\alpha}$ $[\bar{1}\bar{1}\bar{1}]_{\beta} // [11\bar{2}0]_{\alpha}$	$\begin{bmatrix} 1.0082 & 0.0953 & 0.0186 \\ 0.0031 & 1.0258 & -0.0054 \\ 0.0186 & -0.1651 & 0.9867 \end{bmatrix}$	$60.832^{\circ} // (\bar{1}.377 \bar{1} 2.377 0.359)$
V6	$(101)_{\beta} // (0001)_{\alpha}$ $[\bar{1}\bar{1}\bar{1}]_{\beta} // [11\bar{2}0]_{\alpha}$	$\begin{bmatrix} 0.9395 & -0.0562 & -0.0829 \\ -0.0562 & 0.9792 & -0.0586 \\ 0.0677 & 0.0479 & 1.1020 \end{bmatrix}$	$90^{\circ} // (1 \bar{2}.38 1.38 0)$
V7	$(\bar{1}10)_{\beta} // (0001)_{\alpha}$ $[\bar{1}\bar{1}\bar{1}]_{\beta} // [11\bar{2}0]_{\alpha}$	$\begin{bmatrix} 1.0680 & 0.0695 & -0.1419 \\ -0.0227 & 0.9792 & 0.0780 \\ 0.0087 & 0.0247 & 0.9735 \end{bmatrix}$	$(\bar{1}.377 \bar{1} 2.377 0.359)$
V8	$(\bar{1}0\bar{1})_{\beta} // (0001)_{\alpha}$ $[11\bar{1}]_{\beta} // [11\bar{2}0]_{\alpha}$	$\begin{bmatrix} 1.0082 & 0.0953 & -0.0186 \\ 0.0031 & 1.0258 & 0.0054 \\ -0.0186 & 0.1651 & 0.9867 \end{bmatrix}$	$10.5288^{\circ} // (0001)$
V9	$(011)_{\beta} // (0001)_{\alpha}$ $[\bar{1}\bar{1}\bar{1}]_{\beta} // [11\bar{2}0]_{\alpha}$	$\begin{bmatrix} 1.0082 & 0.0953 & -0.0186 \\ 0.0031 & 1.0258 & 0.0054 \\ -0.0186 & 0.1651 & 0.9867 \end{bmatrix}$	$60.832^{\circ} // (\bar{1}.377 \bar{1} 2.377 0.359)$
V10	$(0\bar{1}\bar{1})_{\beta} // (0001)_{\alpha}$ $[\bar{1}\bar{1}\bar{1}]_{\beta} // [11\bar{2}0]_{\alpha}$	$\begin{bmatrix} 1.0548 & -0.0134 & 0.0011 \\ 0.0789 & 0.9792 & 0.0193 \\ -0.1495 & 0.0726 & 0.9867 \end{bmatrix}$	$63.2618^{\circ} // (\bar{1}0 5 5 \bar{3})$
V11	$(\bar{1}10)_{\beta} // (0001)_{\alpha}$ $[111]_{\beta} // [11\bar{2}0]_{\alpha}$	$\begin{bmatrix} 0.9395 & -0.0562 & 0.0829 \\ -0.0562 & 0.9792 & 0.0568 \\ -0.0677 & -0.0479 & 1.1020 \end{bmatrix}$	$90^{\circ} // (1 \bar{2}.38 1.38 0)$

**Fig. 12.** Atomic correspondences between the  $\beta$  phase, the major  $\alpha$  plate and the penetrating  $\alpha$  under the BOR between the  $\beta$  phase and the major  $\alpha$  plate  $(110)_{\beta} // (0001)_{\alpha}$   $[\bar{1}\bar{1}\bar{1}]_{\beta} // [11\bar{2}0]_{\alpha}$ , and the  $60^{\circ} // [\bar{1}2\bar{1}0]_{\alpha}$  rotation between the major  $\alpha$  and the penetrating  $\alpha$ .seen in Fig. 8(a<sub>2</sub>).

## 5. Summary

In the present work, the lattice strain to realize the structure change from the BCC structure of the  $\beta$  phase to the HCP of the  $\alpha$

phase in a metastable  $\beta$  Ti alloy (Ti 7333) and its impact on the formation of the composite structure of the  $\alpha$  precipitates and on local variant selection were thoroughly investigated.

The elastic strain generated by the  $\beta$  to  $\alpha$  transformation induces the formation of two kinds of nano sized  $\alpha$  domains in each major  $\alpha$  plate. This demonstrates that the  $\alpha$  plates are rather polycrystalline

**Table 5**

Deformation gradient tensor of the penetrating  $\alpha$  expressed in the same BOR reference frame as for the major  $\alpha$  plate in Table 2.

Deformation gradient tensor		
0.8984	-0.1039	0.0248
-0.2860	0.8675	0.0421
-0.2617	-0.4532	1.0778

than monocrystalline as has traditionally been considered. One kind of domains forms at the interfaces between the major  $\alpha$  plate and the  $\beta$  matrix (interface  $\alpha$ ). Such domains respect the BOR with the  $\beta$  matrix and related to the major  $\alpha$  by a  $60^\circ/\langle 1\bar{1}20 \rangle_\alpha$  rotation. The formation of such  $\alpha$  domains can effectively accommodate the shear strain and one component of the normal strain present at the interface between the major  $\alpha$  plate and the  $\beta$  matrix. The geometrical characteristics of the lattice strain of such  $\alpha$  domains allow a maximum profit from the low CRSS slip systems of the major  $\alpha$  plate and the  $\beta$  to minimize the overall strain. These domains further serve as sympathetic nuclei for the formation of the other major  $\alpha$  plate with the same orientation and contribute to the formation of the triangular structured major  $\alpha$  plate clusters.

The other  $\alpha$  domains (penetrating  $\alpha$ ) are in lamellar shape and organized into parallel bands going through the major  $\alpha$  plate. The broad faces of the bands are roughly normal to one of the large normal strains generated by the major  $\alpha$  plate. These  $\alpha$  domains are related with the major  $\alpha$  by a  $60^\circ/\langle 1120 \rangle_\alpha$  rotation but it does not obey the BOR with the  $\beta$  matrix. The formation of the bands of the penetrating  $\alpha$  domains is to accommodate the larger extension strain from the major  $\alpha$  plate. As these domains also generate large incompatible strains either with the major  $\alpha$  plate or with the  $\beta$  matrix, their growth are largely confined, thus each band is formed by the aligned and equally spaced identical penetrating  $\alpha$  domains.

The results of the present work provide new information on the displacive characters of the  $\beta$  to  $\alpha$  phase transformation and its impact on the sub structure and the microstructure features of the product  $\alpha$  phase. Such information can be incorporated to simulation models for  $\beta$  to  $\alpha$  transformation of Ti alloys.

## Acknowledgements

The authors gratefully acknowledge the support from the National Natural Science Foundation of China (Grant No. 51371143), the Major State Research Development Program of China (2016YFB0701303), and the Programme de Recherche Conjoint CNRS/National Natural Science Foundation of China (PRC CNRS/NSFC) (Grant Nos. 5161101270 and 228294) to this work. The first author Ke Kua is grateful to the China Scholarship Council for the support to his PhD study in France.

## References

- [1] A.F. Gerday, M. Ben Bettaieb, L. Duchène, N. Clément, H. Diarra, A.M. Habraken, Interests and limitations of nanoindentation for bulk multiphase material identification: application to the  $\beta$  phase of Ti-5553, *Acta Mater.* 57 (2009) 5186–5195.
- [2] Y.F. Zheng, R.E.A. Williams, D. Wang, R. Shi, S. Nag, P. Kami, J.M. Sosa, R. Banerjee, Y. Wang, H.L. Fraser, Role of  $\omega$  phase in the formation of extremely refined intragranular  $\alpha$  precipitates in metastable  $\beta$ -titanium alloys, *Acta Mater.* 103 (2016) 850–858.
- [3] C.M. Liu, X.J. Tian, H.B. Tang, H.M. Wang, Microstructural characterization of laser melting deposited Ti 5Al-5Mo 5V 1Cr 1Fe near  $\beta$  titanium alloy, *J. Alloys Compd.* 572 (2013) 17–24.
- [4] N. Jones, R. Dashwood, D. Dye, M. Jackson, Thermomechanical processing of Ti 5Al 5Mo 5V 3Cr, *Mater. Sci. Eng. A* 490 (2008) 369–377.
- [5] V. Shevel'kov, Structural conversions in VT22 titanium alloy during aging, *Mater. Sci. Eng. A* 34 (1992) 534–539.
- [6] M. Salib, J. Teixeira, L. Germain, E. Lamielle, N. Gey, E. Aebly-Gautier, Influence of transformation temperature on microtexture formation associated with  $\alpha$  precipitation at  $\beta$  grain boundaries in a  $\beta$  metastable titanium alloy, *Acta Mater.* 61 (2013) 3758–3768.
- [7] W.G. Burgers, On the process of transition of the cubic-body-centered modification into the hexagonal-close-packed modification of zirconium, *Physica* 1 (1934) 561–586.
- [8] J.W. Cahn, G.M. Kalonji, Symmetry in solid-solid transformation morphologies, in: P.A. Pittsburgh, H.I. Aaronson, et al. (Eds.), *Proceedings of an International Conference on Solid-solid Phase Transformations*, AIME Press, New York, 1982, p. 3.
- [9] S.M.C. van Bohemen, J. Sietsma, S. van der Zwaag, Experimental observations elucidating the mechanisms of structural bcc-hcp transformations in  $\beta$ -Ti alloys, *Phys. Rev. B* 74 (2006) 134114.
- [10] T. Furuhashi, S. Takagi, H. Watanabe, T. Maki, Crystallography of grain boundary  $\alpha$  precipitates in a  $\beta$  titanium alloy, *Metall. Mater. Trans. A* 27 (1996) 1635–1646.
- [11] D. Banerjee, J.C. Williams, Perspectives on titanium science and technology, *Acta Mater.* 61 (2013) 844.
- [12] D. Bhattacharyya, G.B. Viswanathan, R. Denkenberger, D. Furrer, H.L. Fraser, The role of crystallographic and geometrical relationships between alpha and beta phases in an alpha/beta titanium alloy, *Acta Mater.* 51 (2003) 4679–4691.
- [13] D. Bhattacharyya, G.B. Viswanathan, H.L. Fraser, Crystallographic and morphological relationships between  $\beta$  phase and the Widmanstätten and allotriomorphic  $\alpha$  phase at special  $\beta$  grain boundaries in an  $\alpha/\beta$  titanium alloy, *Acta Mater.* 55 (2007) 6765–6778.
- [14] N. Stanford, P.S. Bate, Crystallographic variant selection in Ti-6Al-4V, *Acta Mater.* 52 (2004) 5215–5224.
- [15] S.M.C. van Bohemen, A. Kamp, R.H. Petrov, L.A.I. Kestens, J. Sietsma, Nucleation and variant selection of secondary  $\alpha$  plates in a  $\beta$  Ti alloy, *Acta Mater.* 56 (2008) 5907–5914.
- [16] E. Lee, R. Banerjee, S. Kar, D. Bhattacharyya, H.L. Fraser, Selection of  $\alpha$  variants during microstructural evolution in  $\alpha/\beta$  titanium alloy, *Phil Mag.* 87 (2007) 3615–3627.
- [17] H. Moustahfid, M. Humbert, M.J. Philippe, Modeling of the texture transformation in a Ti-64 sheet after hot compression, *Acta Mater.* 45 (1997) 3785–3790.
- [18] N. Gey, M. Humbert, M.J. Philippe, Y. Combres, Investigation of the  $\alpha$ - and  $\beta$ -texture evolution of hot rolled Ti-64 products, *Mater. Sci. Eng. A* 219 (1996) 80–88.
- [19] S.C. Wang, M. Aindow, M.J. Starink, Effect of self-accommodation on  $\alpha/\alpha$  boundary populations in pure titanium, *Acta Mater.* 51 (2013) 2485–2503.
- [20] S. Nag, R. Banerjee, R. Srinivasan, J.Y. Hwang, M. Harper, H.L. Fraser,  $\omega$ -Assisted nucleation and growth of  $\alpha$  precipitates in the Ti 5Al 5Mo 5V 3Cr 0.5Fe  $\beta$  titanium alloy, *Acta Mater.* 57 (2009) 2136–2147.
- [21] R. Shi, Y. Wang, Variant selection during  $\alpha$  precipitation in Ti 6Al 4V under the influence of local stress—a simulation study, *Acta Mater.* 61 (2013) 6006–6024.
- [22] R. Shi, V. Dixit, H.L. Fraser, Y. Wang, Variant selection of grain boundary  $\alpha$  by special prior  $\beta$  grain boundaries in titanium alloys, *Acta Mater.* 75 (2014) 156–166.
- [23] R. Shi, N. Ma, Y. Wang, Predicting equilibrium shape of precipitates as function of coherency state, *Acta Mater.* 60 (2012) 4172–4184.
- [24] M. Naoki, N. Takahiro, I. Teruhiko, A. Kei, Reasons for formation of triangular  $\alpha$  precipitates in Ti 15V 3Cr 3Sn 3Al titanium alloy, *Mater. Trans.* 47 (2006) 341–347.
- [25] X. Zhang, H.C. Kou, J.S. Li, F.S. Zhang, L. Zhou, Evolution of the secondary  $\alpha$  phase morphologies during isothermal heat treatment in Ti-7333 alloy, *J. Alloys Compd.* 577 (2013) 516–522.
- [26] K. Hua, J.S. Li, H.C. Kou, J.K. Fan, M. Sun, B. Tang, Phase precipitation behavior during isothermal deformation in  $\beta$ -quenched near beta titanium alloy Ti-7333, *J. Alloys Compd.* 671 (2016) 381–388.
- [27] C. Randau, U. Garbe, H.-G. Brokmeier, StressTextureCalculator: a software tool to extract texture, strain and microstructure information from area-detector measurements, *J. Appl. Crystallogr.* 44 (2011) 641–646.
- [28] J.J. Fundenberger, A. Morawiec, E. Bouzy, J.S. Lecomte, Polycrystal orientation maps from TEM, *Ultramicroscopy* 96 (2003) 127–137.
- [29] A. Morawiec, J.J. Fundenberger, E. Bouzy, J.S. Lecomte, EP—a program for determination of crystallite orientations from TEM Kikuchi and CBED diffraction patterns, *J. Appl. Crystallogr.* 35 (2002), 287–287.
- [30] Y.D. Zhang, S.Y. Wang, C. Esling, J. Lecomte, C. Schuman, X. Zhao, L. Zuo, A method to identify dislocations in a known crystal structure by transmission electron microscopy, *J. Appl. Crystallogr.* 44 (2011) 1164–1168.
- [31] Crystal Maker software, <http://www.crystallmaker.com/>.
- [32] P. Villars (Ed.), *Pearson's Handbook Desk Edition*, ASM International, 1997.
- [33] S.K. Kara, A. Ghosha, N. Fulzele, A. Bhattacharjee, Quantitative microstructural characterization of a near beta Ti alloy, Ti-5553 under different processing conditions, *Mater. Charact.* 81 (2013) 37–48.
- [34] A. Dehghan-Manshadi, R.J. Dippenaar, Development of  $\alpha$ -phase morphologies during low temperature isothermal heat treatment of a Ti 5Al 5Mo 5V 3Cr alloy, *Mater. Sci. Eng. A* 528 (2011) 1833–1839.
- [35] G. Lutjering, J.C. Williams, *Titanium*, Berlin, Springer Berlin Heidelberg, Heidelberg, 2007.
- [36] D. Qiu, R. Shi, D. Zhang, W. Lu, Y. Wang, Variant selection by dislocations during  $\alpha$  precipitation in  $\alpha/\beta$  titanium alloys, *Acta Mater.* 88 (2015) 218–231.
- [37] R. Shi, V. Dixit, G.B. Viswanathan, H.L. Fraser, Y. Wang, Experimental

- assessment of variant selection rules for grain boundary  $\alpha$  in titanium alloys, *Acta Mater.* 102 (2016) 197–211.
- [38] T. Inamura, M. Ii, M. Tahara, H. Hosoda, Formation process of the incompatible martensite microstructure in a beta-titanium shape memory alloy, *Acta Mater.* 124 (2017) 351–359.
- [39] S. Balachandran, A. Kashiwar, A. Choudhury, D. Banerjee, R. Shi, Y. Wang, On variant distribution and coarsening behavior of the  $\alpha$  phase in a metastable  $\beta$  titanium alloy, *Acta Mater.* 106 (2016) 374–387.
- [40] Y.M. Jin, G.J. Weng, A direct method for the crystallography of martensitic transformation and its application to TiNi and AuCd, *Acta Mater.* 50 (2002) 2967–2987.
- [41] K.E.K. Amouzou, T. Richeton, A. Roth, M.A. Lebyodkin, T.A. Lebedkina, Micromechanical modeling of hardening mechanisms in commercially pure  $\alpha$ -titanium in tensile condition, *Int. J. Plast.* 80 (2016) 222–240.
- [42] B. Barkia, V. Doquet, J.P. Couzinié, I. Guillot, E. Héripré, In situ monitoring of the deformation mechanisms in titanium with different oxygen contents, *Mater. Sci. Eng. A* 636 (2015) 91–102.
- [43] M.P. Echlin, J.C. Stinville, V.M. Miller, W.C. Lenthe, T.M. Pollock, Incipient slip and long range plastic strain localization in microtextured Ti-6Al-4V titanium, *Acta Mater.* 114 (2016) 164–175.
- [44] A. Fitzner, D.G.L. Prakash, J.Q. Fonseca, M. Thomas, S.Y. Zhang, J. Kelleher, P. Manuel, M. Preuss, The effect of aluminium on twinning in binary alpha-titanium, *Acta Mater.* 103 (2016) 341–351.